International Journal of Nanomedicine

Dovepress
open access to scientific and medical research

Open Access Full Text Article

ORIGINAL RESEARCH

Enhancing the Biopharmacological Characteristics of Asperosaponin VI: Unveiling Dynamic Self-Assembly Phase Transitions in the Gastrointestinal Environment

Yulin Mo[1,*], Yanjun Yang[1,*], Jingqi Zeng[1], Weikun Ma[1], Yuxin Guan[1], Jingxi Guo[1], Xiaochun Wu[1], Dingkun Liu[1], Liang Feng[1,2], Xiaobin Jia[1,2], Bing Yang[1,2]

[1]School of Traditional Chinese Pharmacy, China Pharmaceutical University, Nanjing, 211198, People's Republic of China; [2]State Key Laboratory of Natural Medicines, China Pharmaceutical University, Nanjing, 211198, People's Republic of China

*These authors contributed equally to this work

Correspondence: Xiaobin Jia; Bing Yang, School of Traditional Chinese Pharmacy, China Pharmaceutical University, Nanjing, 211198, People's Republic of China, Email jiaxiaobin2015@163.com; 15751151582@163.com

Purpose: Asperosaponin VI (ASP VI) as an active ingredient of *Dipsacus asperoides*, which has a wide range of biological and pharmacological activity. However, its development and application are restricted due to the poor gastrointestinal permeability and oral bioavailability. This investigation aims to reveal the influence of the self-assembled structure by the interaction between ASP VI and endogenous components NaTC and/or DOPC in the gastrointestinal environment on its biopharmaceutical properties, and novelty elucidated the molecular mechanism for the formation of self-assembled nanomicelles.

Methods: This change in phase state in gastrointestinal fluids is characterized by dynamic light scattering (DLS) and transmission electron microscope (TEM). UPLC-Q-TOF-MS was used to analyze the composition of phase components and the exposure of nanomicelles in vivo. Molecular dynamics simulation (MDS) was applied to preliminarily elucidate the self-assembly mechanism of ASP VI in the gastrointestinal environment. Furthermore, theS8 promoting absorption mechanism of nanomicelles were investigated through in vivo pharmacokinetic experiments, parallel artificial membrane permeability assay (PAMPA), quadruple single-pass intestinal perfusion in rats, and Caco-2 cell monolayer model.

Results: We demonstrated that the ASP VI could spontaneously form dynamic self-assembled structures with sodium taurocholate (NaTC) and dipalmitoyl phosphatidylcholine (DOPC) during gastrointestinal solubilization, which promoted the gastrointestinal absorption and permeability of ASP VI and increased its exposure in vivo, thus improving the biopharmacological characteristics of ASP VI. Moreover, ASP VI-NaTC-DOPC-self-assembled nanostructures (ASP VI-NaTC-DOPC-SAN) manifested higher cellular uptake in Caco-2 cells as evidenced by flow cytometry and confocal microscopy, and this study also preliminarily revealed the mechanism of self-assembly formation of ASP VI with endogenous components NaTC and DOPC driven by electrostatic and hydrogen bonding interactions.

Conclusion: This study provides evidence that the dynamic self-assembled phase transition may play a key role in improving the biopharmacological characteristics of insoluble or low permeability active ingredients during the gastrointestinal dissolution of Chinese medicines.

Keywords: Asperosaponin VI, dynamic self-assembled structure, gastrointestinal environment, biopharmacological characteristics, oral bioavailability

Introduction

Many drugs exhibit various limitations, including low solubility, poor permeability, unstable nature, rapid metabolism, and significant side effects, which ultimately lead to low bioavailability and unsatisfactory therapeutic outcomes.[1] To enhance the permeability and effectiveness of drugs, nano-delivery systems are extensively employed to improve their

Received: 13 September 2023
Accepted: 27 November 2023
Published: 6 December 2023

Graphical Abstract

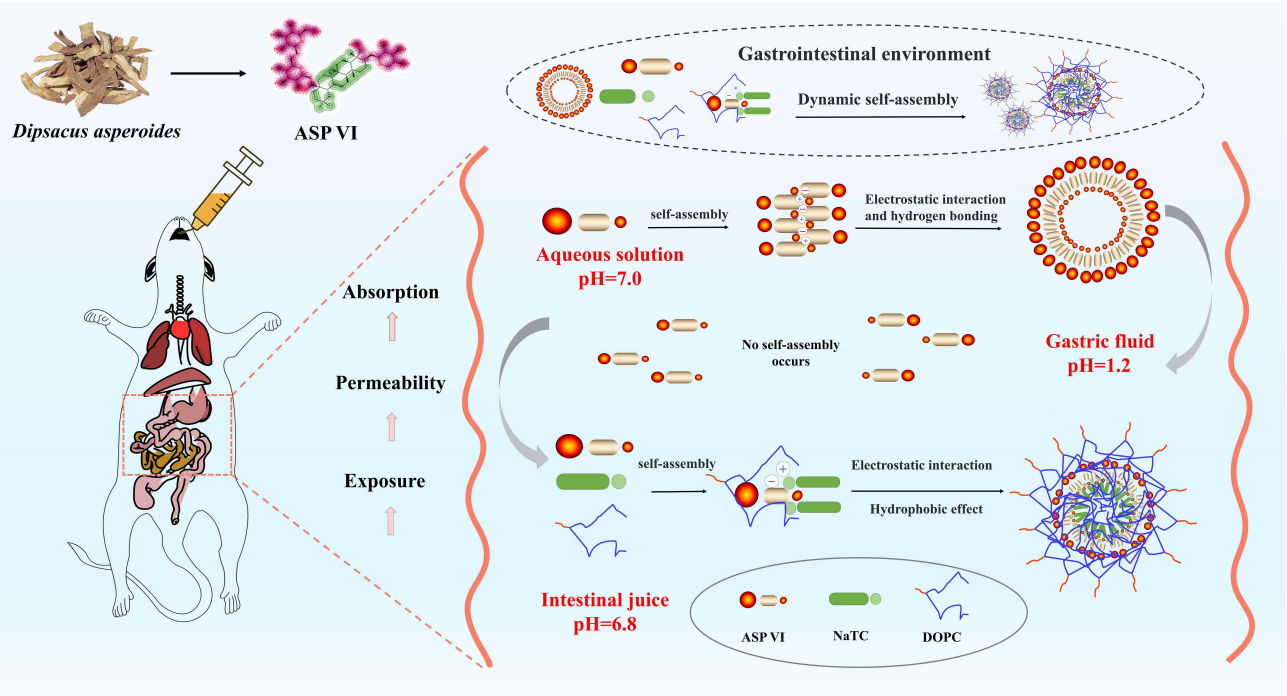

bioavailability.[2] Nano drug delivery systems that have been extensively researched encompass liposomes, biomimetic hybrid micelles, nanoparticles, extracellular vesicles, metal-organic skeletons, and polymeric nano-formulations.[3–5] However, many of these nanocarrier formulation face challenges such as low encapsulation rates, complex synthesis methods, and unpredictable biotoxicity (Table 1).[6] Biomimetic mixed micelles offer superior applicability and can be extensively utilized for both water-soluble and fat-soluble drugs.[7] They possess several advantages, including high drug

Table 1 Comparison of Different Characteristics of Various Nano-Delivery Systems in Drug Delivery and Biomedical Applications

Nano-Delivery System	Advantage	Disadvantage
Liposomes	High biocompatibility and low toxicity	Easily phagocytosed and cleared; Short half-life; Limited drug load
Nanoparticles	Encapsulate water-soluble and fat-soluble drugs	Easily cleared from the body; Uneven drug release
Extracellular vesicles	Natural source; Good biocompatibility; Modulate immune response	Difficult to prepare on a large scale; Relatively low drug loading
Metal–organic framework	High drug loading capacity; Good biocompatibility; Highly tunable structure	Complex preparation process; Uncertain stability and toxicity in organisms
Polymer nano-formulation	Adjustable drug release; Good biocompatibility; High stability and adjustable drug loading capacity	Complicated preparation process; Degradation products of polymers have an impact on organisms
Hydrogels	Good biocompatibility; Local delivery of drugs	Limited drug release rate; Not suitable for all types of drugs
Chitosan nanocarriers	Good biocompatibility; Adjustable drug release rate	Relatively low drug loading; Complicated preparation
Biomimetic mixed micelles	Suitable for water-soluble and liposoluble drugs; Surface adjustable; Higher drug loading; Good biocompatibility	Complicated preparation

Note: Data from Park et al.[6]

loading rate and biological safety. The formation of stable nanomicelles through direct self-assembly of endogenous components and small molecules using noncovalent supramolecular forces such as hydrogen bonding, van der Waals forces, and electrostatic interactions has gained significant attention from researchers in recent years.[8] A typical study among them is the application of bile salt/phospholipid biomimetic mixed micelles are more widely used due to its outstanding solubilizing ability for water-insoluble drugs such as glycyrrhetinic acid, ginsenoside and silybin.[9]

Numerous studies have consistently demonstrated that endogenous surfactants present in human intestinal fluid can spontaneously form nanophase states. These nanophase states have the potential to improve drug solubility, membrane permeability, and bioavailability. Although intestinal fluid primarily consists of water, it also contains various bile salts, phospholipids, and cholesterol, making it a complex colloidal solution. NaTC is the most abundant bile salt, accounting for 85% of the total, and is commonly used as a representative for all bile salts.[10] Similarly, lecithin (usually DOPC) is used as a representative for all phospholipids. According to the synergistic effect theory, mixed micelle systems formed by combining two or more materials exhibit superior characteristics compared to traditional micelles composed of a single carrier material. Bile salts, which are anionic surfactants, possess excellent solubility and biocompatibility. They play a crucial role in various physiological and biological systems known as "physiological detergents".[11] In drug delivery studies, it is commonly accepted that elastic nanoparticles with a low Young's moduli (45–71 kPa) demonstrate enhanced cellular uptake and drug accumulation in the body. DOPC has soft and flexible properties due to its long lipid tail chain, which helps to improve the biocompatibility of nanostructured surfaces.[12] Choosing NaTC and DOPC as carrier materials to investigate the influence of endogenous components on the absorption and bioavailability of bioactive substances is essential for guiding the optimization of nano-formulation and precise clinical medication.

Asperosaponin VI (ASP VI), an active saponin component extracted from *Dipsacus asperoides*, has been proven to hold the pharmacological activity against osteoporosis.[13–15] Notwithstanding, ASP VI belongs to Biopharmaceutics Classification System class III (high solubility/low permeability) with poor oral bioavailability (<0.13%) and strong hydrophilic properties. These properties are attributed to its physical properties such as high molecular weight (>500 Da) and a large number of hydrogen bonds (>12),[16] exhibiting amphipathic properties that easily form the self-assembled structures. Numerous studies have shown that the active ingredients with different amounts of hydroxyl and carboxyl groups could spontaneously self-assemble into nanomicelles through non-covalent interactions such as π-π stacking, electrostatic interactions, hydrogen bonding and coordination to change its mucosal permeability.[17–19] However, whether ASP VI can form self-assembled structures with NaTC and/or DOPC under gastrointestinal physiological conditions to improve the biopharmaceutical properties of ASP VI and enhance its anti-osteoporosis effect, and the underlying mechanism of this interaction is still unclear.

This investigation aims to reveal the influence of the self-assembled structure by the interaction between ASP VI and endogenous components NaTC and DOPC in the gastrointestinal environment on its biopharmaceutical properties, and novelty elucidated the molecular mechanism for the formation of self-assembled nanomicelles (Figure 1), aiming to enhance the bioavailability of ASP VI in vivo.

Materials and Methods

Materials

Dipsacus asperoides Bone-enhancing Capsule was purchased from Zhejiang Di'er Pharmaceuticals Company. Asperosaponin VI (ASP VI, ≥98%) was supplied by Sichuan Weikeqi Biological Technology Corporation. Sodium taurocholate was purchased from Beijing Bailingwei Technology Company (NaTC, 98%). Dipalmitoyl phosphatidylcholine was purchased from Shanghai McLean Biochem Company (DOPC, 97%). L-glutamine, non-essential amino acids, fetal bovine serum and penicillin–streptomycin–amphotericin B were obtained from Gibco (Maryland, USA). DiO, Hoechst and Lyso-tracker red were purchased from Beyotime Biotechnology Company. Pancreatic enzyme (PE, potency≥250 units/mg), egg yolk phosphatidylcholine (EYPC, ≥80%) and dodecane (DDC, ≥99%), cholesterol, simvastatin, genistein and methyl-*β*-cyclodextrin were purchased from Aladdin Biochem Technology Company (Shanghai, China).

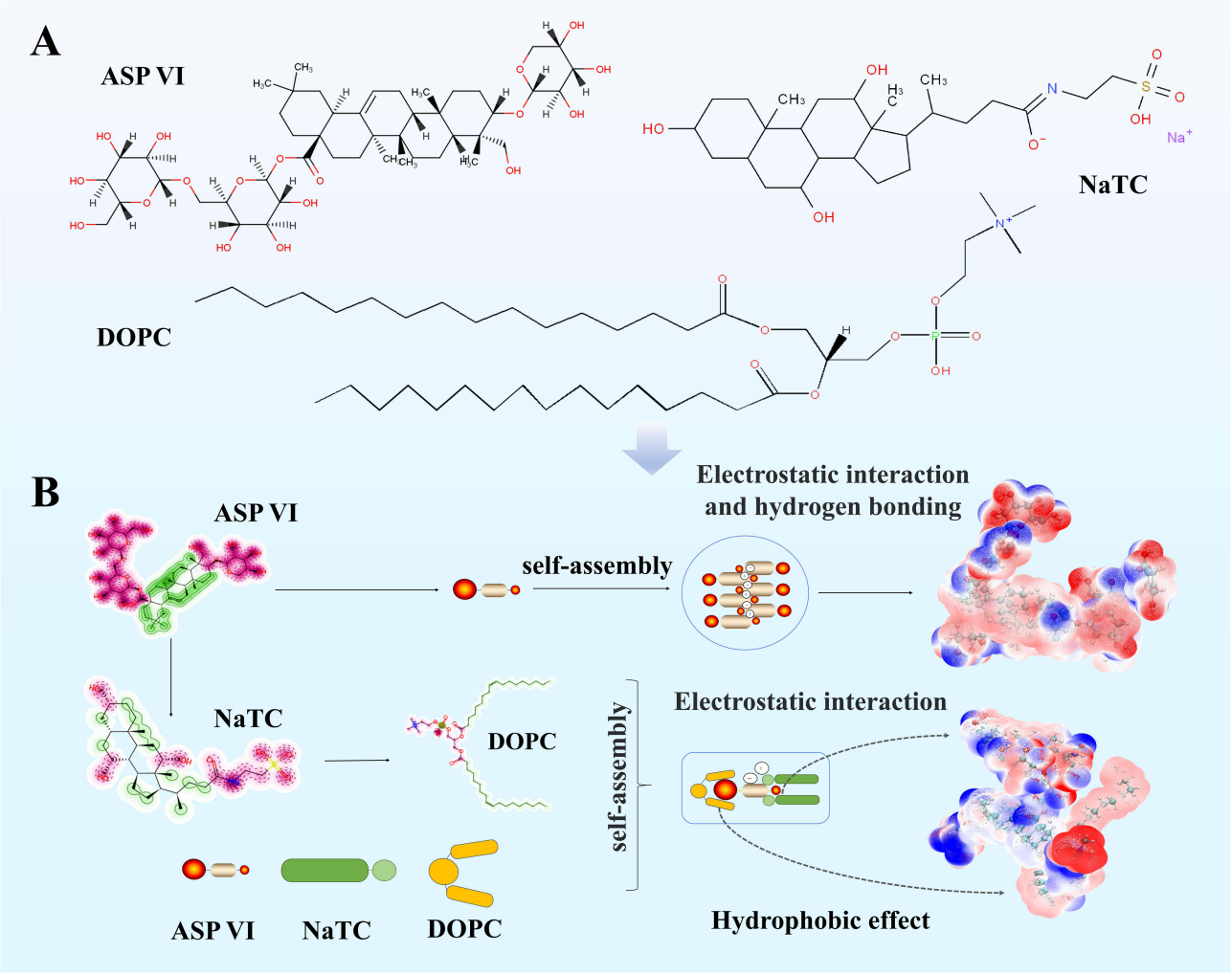

Figure 1 Schematic diagram of self-assembly of ASP VI with NaTC and/or DOPC. (**A**) Chemical structure of ASP VI, NaTC and DOPC; (**B**) Schematic diagram of the self-assembly process of ASP VI with NaTC and DOPC.

Human colon adenocarcinoma Caco-2 cell line was obtained from Shanghai Yuchun Biology Science and technology, Lot Number: 20220221-15, ampule passage number 10. Cells were grown in MEM with 20% fetal bovine serum (FBS) medium supplemented with 4 mM L-glutamine, 1% non-essential amino acids (NEAA) and 1% penicillin–streptomycin–amphotericin B (10,000 units penicillin, 10 mg streptomycin, and 25 μg amphotericin B per mL). These cells were maintained at 37 °C in a humidified incubator containing 5% CO_2.

SPF-grade male Sprague Dawley (SD) rats weighing 300±20 g was supplied by Zhejiang Chinese Medical University with a permit number of SCXK (Zhe) 2019–0002. All rats were fasted for 16 hours with free access to water prior to the experiments. Conducting animal experiments were approved by the Committee on Animal Protection of China Pharmaceutical University, according to all applicable international, national and institutional guidelines for animal care and use. The experiment was performed strictly, following the International Guidelines for Animal Welfare.

Bionic Digestion Simulation in vitro

The simulated gastric fluid (SGF), simulated duodenum fluid (SDF), simulated jejunum fluid (SJF), simulated ileum fluid (SIF) and simulated colonic fluid (SCF) were separately prepared according to a simulated digestion system previously reported in literature,[20–22] (Tables S1 and S2). Thirty milliliters of simulated gastric and intestinal fluids were incubated individually in 37 °C water bath for 30 minutes. The *Dipsacus asperoides* water extract was freeze-dried to obtain the powder and then added into 6 systems (simulated gastric, duodenal, jejunal, ileal, colonic and aqueous solutions) with

a stir of 40 rpm at 37 °C. Six different sets of mixed solutions were obtained by the above experiments respectively. After centrifugation at 3000 rpm for 10 minutes, the supernatant was collected and removed in a 30-kDa ultrafiltration centrifuge tube and then centrifuged at 3500 rpm for 30 minutes. Methanol of 0.5 mL was added into 0.5 mL blank solution and 0.5 mL nano-phase sample solution respectively, and the composition of in phase solution samples were analyzed by being injected into UPLC-Q-TOF-MS after passing through 0.22 μm microporous membrane. The simulated intestinal fluid was prepared by using a reduction method to simulate the dissolution process and gradually reduce its intrinsic components (Table S3).

Preparation of Self-Assembled Nanomicelles

Firstly, DOPC (45 mg) was dissolved in chloroform (25 mL) in a round-bottomed flask and dried using a rotary evaporation apparatus at 40 °C (water bath) to form a thin phospholipid membrane.[23] The bile salt solution was prepared by dissolving NaTC (105 mg) in simulated intestinal fluid solution (20 mL). The lipid film was mixed with the bile salt solution under ultrasonic conditions (37 °C for 10 minutes) until the mixed solution was clarified to obtain blank micelles. Secondly, blank micelle solution was mixed with ASP VI (200 mg) and stirred using a magnetic stirrer at room temperature for 72 hours for obtaining ASP VI-NaTC-DOPC-SAN.

Typically, micellar solution of 100 mL was obtained and then freeze-dried for storage. During the measurement, it is simply dissolved in the same volume of Milli-Q water.

Dynamic Light Scattering (DLS)

One milliliter of the sample was taken and equilibrated at 37 °C for 2 minutes. The particle size distribution of the sample was determined, including the polydispersity index (PDI), count rate value and zeta potential value (ζ, mV).

Transmission Electron Microscopy (TEM) and Scanning Electron Microscope (SEM)

The sample of 100 μL was dropped onto a 300-mesh copper grid and allowed to stand for 5 minutes, and then stained with 10 μL phosphotungstic acid (2%). The grid was allowed to dry under infrared light conditions for the visualization on an FEI Talos L120C transmission electron microscope with an accelerating voltage of 120 kV under bright field conditions. Meanwhile, the lyophilized samples were observed by using Regulus-8100 SEM (Hitachi Ltd., Tokyo, Japan).

Differential Scanning Calorimetry (DSC)

Samples of 2–5 mg were weighed precisely and analyzed using a NETZSCH DSC 3500 differential scanning calorimeter and the temperature range was from room temperature to 400 °C at a heating rate of 10 °C/min.

Thermogravimetric Analysis (TGA)

TGA analysis of NaTC, DOPC, ASP VI, ASP VI-NaTC-DOPC-PM, and ASP VI-NaTC-DOPC-SAN was performed using PerkinElmer TGA4000 thermal analyzer.

Fourier Transform Infrared (FT-IR) Spectroscopy Analysis

The Bruker TENSOR 27 Fourier transform infrared spectrometer was used for the functional group characterization and structural analysis of NaTC, DOPC, ASP VI, ASP VI-NaTC-DOPC-PM and ASP VI-NaTC-DOPC-SAN in the 4000–400 cm^{-1} range.

Stability of Self-Assembled Nanomicelles

The stability of ASP VI-NaTC-DOPC-SAN was evaluated for their stability in SGF (pH=1.2), SIF (pH = 6.8) and deionized water (control group). After being incubated in SGF and SIF for 0, 0.5, 1, 2, 4 and 6 hours, the SGF incubation solution was neutralized with 0.1 M NaOH to pH=7.4, and then the size, PDI and zeta potential of these nanomicelles were measured. Each group had three repeats and the experiment was repeated three times.

Molecular Dynamics Simulation

Molecular dynamics simulation (MDS) was carried out to prove the self-assembly mechanism. All MDS were performed using Gromacs 2020.6 software.[24] The 2D molecular structures of ASP VI, NaTC and DOPC were obtained from the PubChem database (https://pubchem.ncbi.nlm.nih.gov) and simulated using the gromos54a7 force field and topology files through the Automated Force Field Topology Builder website.[25,26] The simple point charge model was used for water molecules. All hydrogen-containing bonds were constrained using the LINCS algorithm while electrostatic interactions were calculated using the particle-mesh Ewald method.[27] During the process of MDS, a 10 Å non-bonded interaction cutoff was used and the non-bonded list was updated every 10 steps. The method of V-rescale[28] and Parrinello-Rahman[29] were employed for temperature and pressure coupling in the MDS calculations, respectively.

Specifically, the major steps of the experimental procedure are briefly described as follows: Firstly, the system was optimized by the steepest descent method in a vacuum environment, with each cutoff value set to 10 Å to eliminate atomic contacts and the energy minimization convergence value set to 1000.0 kJ/moL/nm. Secondly, position-constrained MDS were performed and equilibrated, allowing only solvent molecules to move, under canonical ensemble and constant-pressure, constant-temperature conditions at 300.0 K and 1.0 bar pressures. The relaxation time of the solvent molecules was set to 10 ps, while the equilibration time was 200 ps in this setting. To obtain a stable conformation of the ASP VI structure, three independent MDS (assigning different initial velocities) were carried out for 40 ns with conformations saved every 10 ps. After the simulation, the spatial position of the small molecule compounds was extracted and the molecular van der Waals surface electrostatic potentials were calculated using the Gaussian 09 software package and the Multiwfn program for quantum chemical wave function analysis.[30,31] Data analysis and visualization of simulation results were performed using Gromacs' built-in program and the VMD1.9.4 program.

PAMPA for Permeability Characterization in vitro

The Parallel artificial membrane permeation model (PAMPA) was performed in the light of the PAMPA-coupled in vitro gastrointestinal digestion model developed by Piazzini[32] and Joaquin.[33] The permeation study in vivo was measured using a vertical cell diffusion with (Franz diffusion cell), composed of a donor compartment with the diffusion area of 2.2 cm^2 and receptor compartment with a volume of 8 mL. A thin layer of artificial membrane was prepared by adding 500 μL of clear 4% (W/V) artificial membrane solution, allowing the solvent to evaporate. The drug molecule solution of 2 mL was added to the upper chamber in a sequence. Samples were taken from the lower chamber at 2, 6, 10, 18, 24, 32 and 48 hours after setting the transdermal apparatus to 37 °C and 300 rpm, respectively, and the drug concentrations were measured to calculate the effective permeability coefficient *Lg* P_e (Equation 1) and effective permeability rate *Teff* (Equation 3), as follows:

$$lgP_e = lg\left\{\frac{V_a V_d}{(V_a + V_d A \cdot t)} \cdot \left[-ln\left(1 - \frac{[drug]_a}{[drug]_e}\right)\right]\right\} \tag{1}$$

$$[drug]_e = \frac{[drug]_d \cdot V_d + [drug]_a \cdot V_a}{V_d + V_a} \tag{2}$$

$$\text{Teff} = \frac{[\text{drug}]\text{a}}{[\text{drug}]\text{e}} * 100\% \tag{3}$$

V_d: the amount of liquid added to the supply plate; V_a: the amount of liquid added to the receiving plate; $A=\pi\times r^2$: the effective area of artificial membrane; *t*: incubation time (s); $[drug]_a$: the drug concentration on the receiving plate at time *t;* $[drug]_e$: the theoretical equilibrium concentration at time *t;* $[drug]_d$: the drug concentration in the supply plate at time *t*.

Quadruple Single-Pass Intestinal Perfusion in Rats

Single-pass intestinal perfusion model,[34] a classical model, was conducted for evaluating the absorption characteristics of drug molecules with a slight adjustment. Reagents such as glucose, calcium chloride and sodium chloride were precisely weighed and dissolved in distilled water to prepare 1L Krebs-Ringer fresh solution. Furthermore, ASP VI (0.75 g) was

dissolved in Krebs-Ringer solution (100 mL) to a final concentration of 7.5 mg/mL. Then, the mixed solution was sonicated for 30 minutes, and centrifuged at 4500 rpm for 15 minutes.

Male SD rats were fasted for 16 h without water and anesthetized with 1.5% sodium pentobarbital (0.2 mL/100 g). An incision of 4–5 cm was made along the midline of the abdomen, and then different intestinal segments including duodenum (1 cm from the pylorus), jejunum (15 cm from the pylorus) and ileum (20 cm from the cecum) were carefully separated from each other. An approximately 10 cm long segment of the intestine was partially cut at both ends, being inserted into a perfusion tube and ligated separately. The digestive contents in the ligated intestinal segment were rinsed at 37 °C with 0.9% physiological saline and then saturated with Krebs-Ringer solution for 10 minutes. The solution in a known weight small bottle, which was maintained at 37 °C and perfused the intestine at a flow rate of 1.0 mL/min for 15 minutes to reach an equilibrium. Subsequently, the flow rate was adjusted to 0.2 mL/min. Perfusion fluid was collected every 15 minutes in the small bottle for 1.5 hours. After the experiment, the weight of the received bottle was measured and the weight of the perfusion solution was calculated after each experiment. The circumference and surface area of the perfused intestinal segment were calculated by measuring its diameter and length. Ultimately, 1 mL aforementioned intestinal perfusion solution was mixed with 1 mL of methanol and vortexed at 2000 rpm for 2 minutes. The supernatant was collected by centrifuging at 12,000 rpm for 5 minutes and then transferred to the sample bottle through a needle filter. The absorption rate constant (K_a) and effective permeability coefficient (P_{eff}) of ASP VI in duodenum, jejunum and ileum were measured according to the following equations:

$$Ka = \left(1 - \frac{C_{out}}{C_{in}} * \frac{Q_{out}}{Q_{in}}\right) * \frac{Q}{\pi r^2 l} \tag{4}$$

$$P_{eff} = -Q(\ln \frac{C_{out}}{C_{in}} * \frac{Q_{out}}{Q_{in}})/2\pi rl \tag{5}$$

Herein, C_{out} is the steady-state concentration of the drug molecules in the intestinal tube, representing the concentration of the drug molecules at the outlet of the intestine; C_{in} is the concentration of the drug molecules in infusion solution prior to entering the intestine; Q is the perfusion rate of 0.2 mL/min; r is the radius of the perfused intestine segment; l is the length of the perfused intestine segment; Q_{in} and Q_{out} refer to the volume of perfused fluid entering and leaving in intestine, respectively. The quantitative method was evaluated according to Herrera et al report.[35] The detailed parameters are described in Table S4.

Cellular Uptake Studies in vitro

Cellular uptake was evaluated using flow cytometry and confocal laser scanning microscopy (CLSM).[36] Caco-2 cells were seeded into observation dishes for CLSM, at a density of 4×10^5 cells/dish. After the cells reached 90% confluence, the medium was exchanged for MEM (FBS-free) containing ASP VI and ASP VI-NaTc-DOPC-SAN labelled with 3.3′-dioctadecyloxacarbocyanine perchlorates (DiO) at 37 °C. After being incubated for 1 h and removed the supernatant, the cells were gently washed three times with PBS for CLSM analysis, and its nuclei was stained with Hoechst 33342 fluorescent dye at 37 °C for 30 minutes. Sequentially, the endosome of cells was stained with Lyso-Tracker Red at 37 °C for 30 minutes. The cells were fixed by 3% glutaraldehyde solution at 4 °C for 30 minutes, and ultimately observed under CLSM (Zeiss LSM880, Carl Zeiss, Oberkochen, Germany).

Quantitative analysis of cellular uptake was performed by flow cytometry (FACS).[37] ASP VI and ASP VI-NaTC-DOPC-SAN (500 μg/mL) labeled with DIO fluorescence was diluted with MEM medium (FBS-free) and co-cultured with Caco-2 cells respectively. Subsequently, the cells were collected by centrifugation for the quantitative analysis (1×10^5 cells) in PBS buffer by FACS.

Systemic Circulation Exposure Study

The rats were randomly assigned into the following three experimental groups: drug-free, ASP VI-NaTC-DOPC-PM and ASP VI-NaTC-DOPC-SAN groups (the content of ASP VI is 150 mg/kg). All rats were anesthetized with 3% sodium pentobarbital (45 mg/kg) and blood samples (0.5 mL, approximately 10 drops) were collected at 5, 15, 30, 45, 60, 120,

240, 360, 480, 600, 720 and 1440 minutes from the retro-orbital plexus using heparin sodium anticoagulant (8 mg/mL) tubes after the administration of drugs. The blood samples were allowed to stand for 30 minutes, then centrifuged at 3000 rpm for 10 minutes, and the supernatant was extracted as plasma samples and stored at −80 °C before further analysis. Take 100 μL of plasma, add 10 μL of internal standard solution (500 ng/mL glycyrrhizic acid methanol solution), 280 μL of methanol, and 10 μL of acetic acid sequentially at room temperature, vortex for 1 minute, and then centrifuge the sample at 14,000 rpm for 15 minutes at 4 °C to precipitate the proteins (20R Microfuge, Beckman coulter, USA).[38] Finally, a 5 μL supernatant was injected into UPLC-Q-TOF-MS for analysis.

Statistical Analysis

Statistical analysis was performed using GraphPad Prism 8.0 (GraphPad Software, Inc.). The data was expressed as means ± standard deviation (SD) in this study. Student's *t* test (two-tail) was performed for analysis of only two groups while one-way Analysis of Variance (ANOVA) for multiple groups. Statistical significance was reported when the calculated *P* value was less than 0.05. All experiments were replicated in the laboratory at least three times.

Results and Discussion

Digestion Characteristics of the Dipsacus Asperoides Water Extract in vitro

The aggregation state composition of the *Dipsacus asperoides* aqueous extract was compared during the process of digestion in vitro (Figure 2A). DLS analysis revealed that the water extract of *Dipsacus asperoides* exhibited an aggregation state in both aqueous solution and digestion solution during the digestion process in vitro. Active ingredients in traditional Chinese medicine (TCM) have been found to easily form aggregates in micromolar concentration.[39] The aggregates formed spontaneously in aqueous solution exhibited a wide range of particle size (Figure 2B). In contrast, the nano-state formed in simulated jejunal juice and ileal juice exhibit more uniform dispersion with PDI less than 0.4 (Figure 2C), mean count rate more than 100 (Figure 2D) and high absolute value of Zeta potential (Figure 2E). It has been reported that the bile salts and phospholipids in the simulated intestinal fluid is able to form micelles with natural component due to its excellent self-assembly capabilities.[40]

UPLC-Q-TOF-MS was used to analyze the nano-state composition of aqueous extracts from *Dipsacus asperoides* in water, simulated gastric and intestinal fluids. *Dipsacus asperoides* saponins (DAS) was the main component in the nano-phase solution of the aqueous extracts from *Dipsacus asperoides*, which included Asperosaponin B, Asperosaponin V, Asperosaponin VI, Asperosaponin VII, Acetyl-asperosaponin VI, and Hederagenin-3-O-*α*-L-araboside pyranoside (Figure S1).[41,42] Notably, the active ingredient ASP VI was identified as the major component. Additionally, bile acids have a natural tendency to form self-assembled supramolecular nanomicelles due to its amphiphilic nature.[43]

Self-Assembled Nanostructures of DAS

The nano-state components of DAS were further analyzed when dissolved in different solutions such as Water, SGF, SIF, SGF and SIF without enzymes. The phase characterization of DAS in SIF was analyzed by transmission electron microscopy. The results showed a significant decrease in particle size and PDI, while Count Rate and Zeta potential showed a significant increase, resulting in the formation of a stable nano-state with an average particle size of 123 nm, PDI of 0.55, and Mean Count Rate of 159 (Figure 3A and B). The phase characterization of the dissolution process of DAS showed a highly consistent with the aqueous extract of *Dipsacus asperoides*, demonstrating the presence of self-assembled nano-state of DAS in intestinal fluid. Furthermore, TEM results demonstrate that the self-assembled nano-micelles formed by DAS in simulated intestinal fluid containing endogenous components have more uniform particle sizes and conform to specific shape rules (Figure 3Evii and viii). This is in contrast to the nanostructures formed in simulated intestinal fluid without endogenous components (Figure 3Ev and vi) and aqueous solution (Figure 3Ei and ii).

It is worth noting that the formation of nanomicelles in the simulated intestinal fluid presented the characteristics of uniform and regular rod-like clumps. However, nanomicelles appeared as gel chain-like aggregates in the artificial gastric fluid (Figure 3Eiii and iv), which may further explain the characteristics of polydispersity and high PDI. It has been revealed that the change of pH value may affect the formation of numerous nanomicelles during TCM decoction and

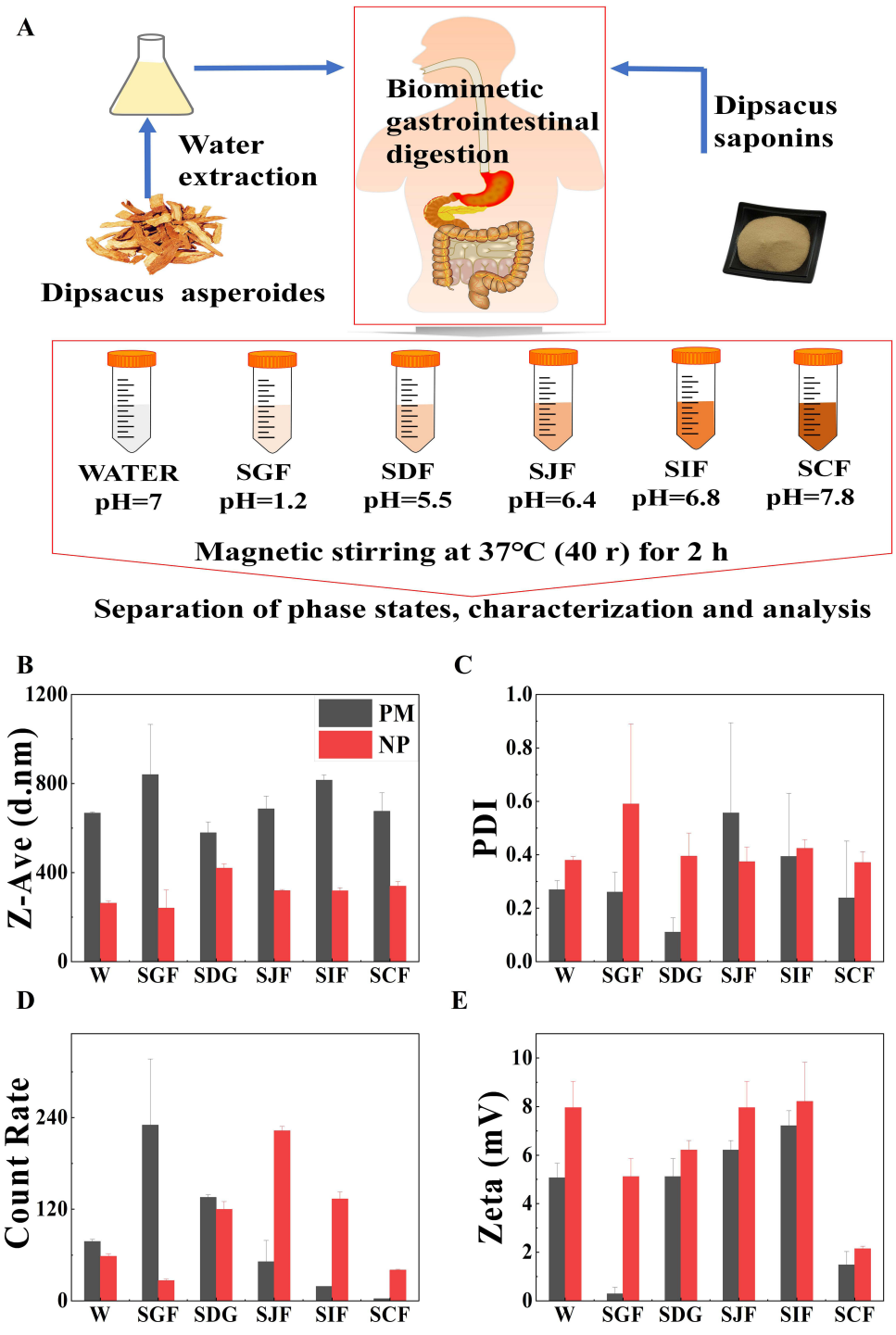

Figure 2 Digestion characteristics of the *Dipsacus asperoides* water extract in vitro. (**A**) Diagram of biomimetic dynamic digestion in vitro, water solution (W), simulated gastric fluid (SGF), simulated duodenal fluid (SDF), simulated empty intestine fluid (SJG), simulated ileum fluid (SIF) and simulated colonic fluid (SCF); (**B**) Particle size of physical mixtures (PM) and nano-phase states (NP); (**C**) PDI of PM and NP; (**D**) Mean count rate of PM and NP; (**E**) Zeta potential of PM and NP (PM and NP formed by aqueous extracts of *Dipsacus asperoides* in different simulation systems).

preparation process.[44] Therefore, we speculated that the self-assembly of DAS may be regulated by pH, namely, it may be easier to form self-assembled nanostructures of uniform size at higher pH conditions. Based on the above findings, we speculated that DAS spontaneously assembled into nanomicelles in aqueous solution in vitro. Under strong acidic

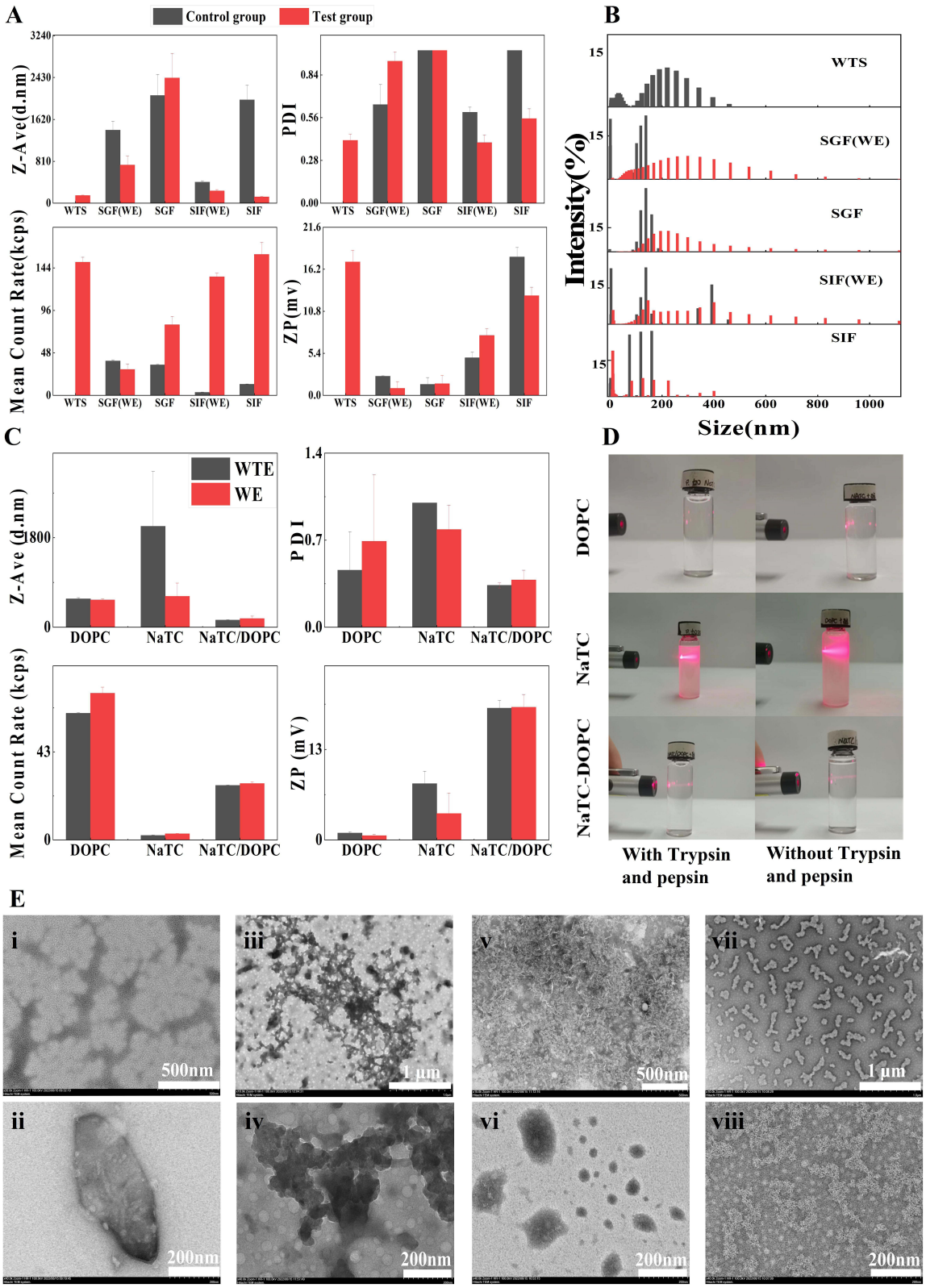

Figure 3 Characterization of nanomicelles formed by the interaction of DAS with endogenous components. (**A**) Particle size, uniformity and stability of nano micelles in different dissolved systems; (**B**) Analysis of particle size distribution of nanomicelles of different dissolved systems, (**C** and **D**) Analysis of the necessary components for the formation of nano phase states, (**E**) TEM analysis of nano phase states in different dissolved systems: (Ei-Eii) TEM characteristics of nano phase states in aqueous solution; (Eiii-Eiv) TEM characteristics of nano phase states in artificial gastric juice; (Ev-Evi) TEM characteristics of nano phase states in artificial intestinal fluid; (Evii-Eviii) TEM characteristics of nano phase states in simulated artificial intestinal fluid (containing endogenous components).

conditions of gastric juice in vivo, the weak bonds of self-assembled structures were broken. However, DAS with endogenous components (NaTC and DOPC) reassembled into a more stable nanomicelles.

Furthermore, six different intestinal solutions of DAS were prepared, which contained DOPC, NaTC and NaTC-DOPC with enzyme, and the above intestinal solutions without enzyme. Then, DLS was used to monitor particle size over the self-assembly process. Interestingly, we found that the enzyme was not involved in the assembly process, but the presence of both NaTC and DOPC were essential components for the formation of NaTC-DOPC-DAS self-assembled structure (Figure 3C). Simultaneously, the results showed that the PDI of NaTC-DOPC and NaTC-DOPC-DAS nanomicelles was the smallest (Figure S2), the particle size distribution was narrowest and exhibiting a strong Tyndall effect (Figure 3D). It is worth noting that the absolute values of Zeta potential and Count Rate of NaTC-DOPC-DAS nanomicelles were significantly increased, compared with the NaTC-DOPC group. Non-significant differences in PDI and particle size indicated that the particle dispersion system of NaTC-DOPC-DAS nanomicelles has a better stability and an enhanced electrostatic effect of the phase state. The differences in findings aforementioned may be attributed to the change of microstructure on the surface of nanomicelles.[45]

Further analyses are required to understand and specify the active components involved in self-assembly of DAS and endogenous components (NaTC and DOPC) more clearly. High performance liquid chromatography was used to resolve the composition of NaTC-DOPC-DAS nano-state solutions, and ASP VI was the main active component involved in the self-assembly of DAS (Figure S3).

Preparation and Characterization of ASP VI Self-Assemblies

ASP VI could self-assemble into a spherical structure of nanomicelles with diameter of 215 ± 2.3 nm and Zeta potential of −14.8 ± 0.6 mV in aqueous solution. However, ASP VI and NaTC-DOPC could be self-assembled into nanomicelles with diameter of 223 ± 14.1 nm and Zeta potential of −47 ± 0.3 mV in intestinal solution (Figure 4A and B). The micelle-forming tendency of ASP VI (0.437 mg/mL) and ASP VI-NaTC-DOPC-SAN (5.12×10^{-2} mg/mL) were confirmed by measuring the critical micelle concentration (CMC) using pyrene as a fluorescent probe (0.437 mg/mL) (Figure 4C and D). The above findings indicated that nanomicelles of ASP VI-NaTC-DOPC could be formed even in a dilute gastrointestinal environment. In addition, a uniform spherical morphology of ASP VI could be clearly observed from the TEM image (Figure 4Ei), while the agglomerated nanomicelles of ASP VI-NaTC-DOPC-SAN were formed with smaller free drug molecules distributed in the periphery (Figure 4Eii). SEM analysis was performed to verify the nanostructures of the two self-assembled micelles. Interestingly, the spherical structures of both ASP VI and ASP VI-NaTC-DOPC-SAN were observed in the image of TEM (Figure 4Eiii and iv), showing an obvious difference between the surface morphology of the ASP VI and ASP VI-NaTC-DOPC-SAN. The self-assembly structure can be influenced by the interaction at the interface, which depends on the surface properties, such as amphiphilicity, electrostatic interactions, and physical properties including microscopic morphology and roughness.[46]

Mechanism of Self-Assembly Structure Formation

MDS of ASP VI Self-Assembly in Aqueous Solution

To further elucidate the self-assembly of ASP VI in aqueous solutions, we next performed MDS to investigate the molecular interactions during the self-assembly processes. The MDS were performed by the Gromacs software[47] under the Amber99SB-ILDN force field.[48] ASP VI molecule of 50 was randomly inserted into a 10×10×10 nm aqueous solution and the system was equilibrated for energy, temperature, pressure and density (Figure S4). Sequentially, the system was subjected to MDS of 40 ns. As depicted in (Figure 5A), the rod-shaped clusters were formed by self-assembly of ASP VI molecules after 10 ns of simulation. Further analysis of the electrostatic potential on the molecular Van der Waals surfaces demonstrated that electrostatic interaction is the mainly driving force for the self-assembly of ASP VI in aqueous solution.

The results of MDS showed that hydrogen bonding plays a crucial role in the self-assembly process of ASP VI in aqueous solution (Figure 5B). This binding force is mainly achieved by increasing the number of hydrogen bonds among cluster molecules and decreasing the number of hydrogen bonds acting on water molecules (Figure 5Bv and vi). An increase of root means square deviation (RMSD) (Figure 5Bi) and a decrease of the radius of rotation (Rg) (Figure 5Bii) and solvent-accessible surface area (SASA-Area) during the simulation indicated that a stable self-assembled nanomicelles structure is formed in the system (Figure 5Biii). However, the decreased solventized-free energy and the lower

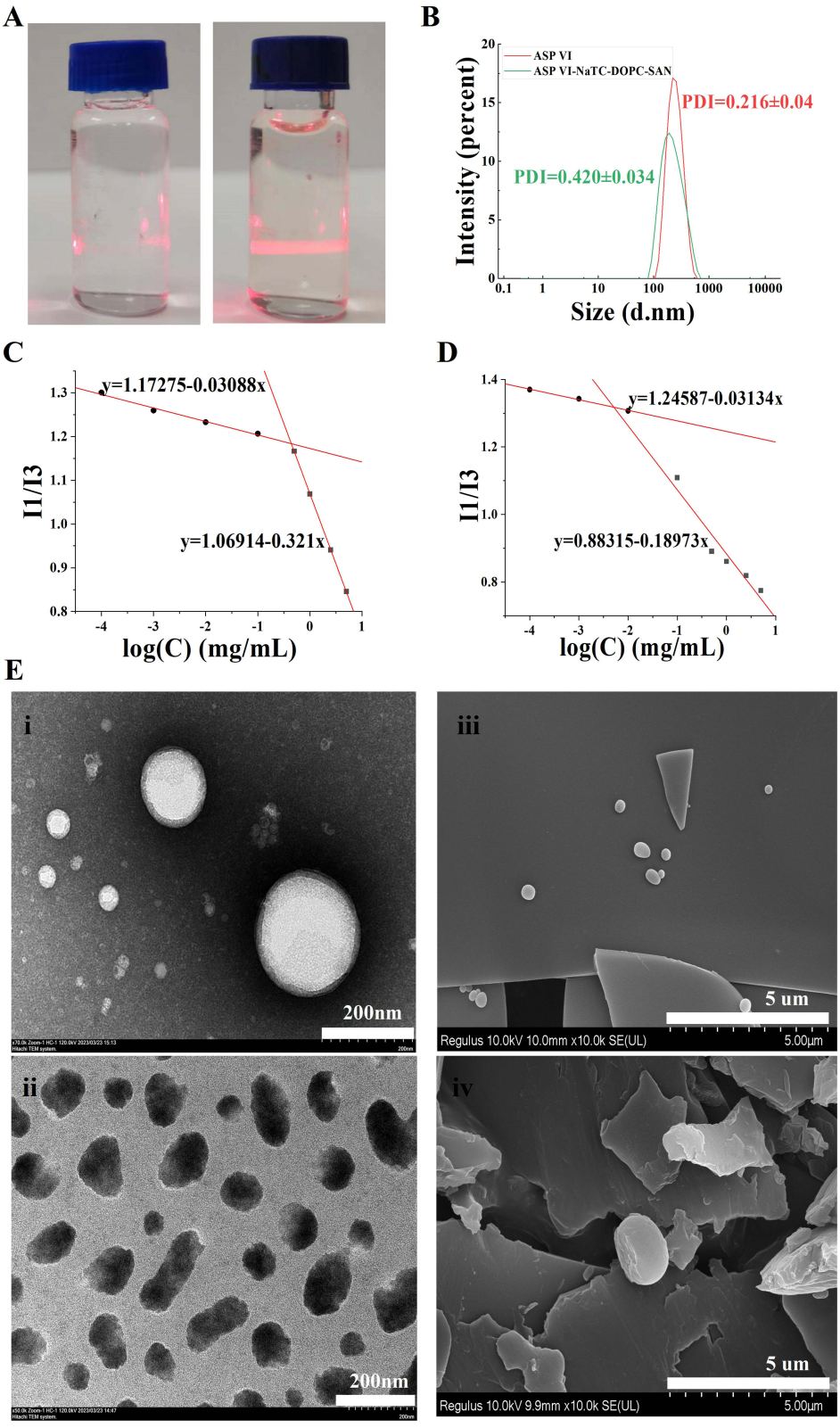

Figure 4 Characterization of ASP VI self-assemblies. (**A**) Dundar effect of ASP VI and ASP VI-NaTC-DOPC-SAN; (**B**) Two self-assembled particle size distributions of ASP VI and ASP VI-NaTC-DOPC-SAN; (**C**) Critical micellar concentration of ASP VI (**D**) Critical micellar concentration of ASP VI-NaTC-DOPC-SAN; (**E**) TEM and SEM characteristics of ASP VI and ASP VI-NaTC-DOPC-SAN: (Ei) TEM analysis of ASP VI; (Eii) TEM analysis of ASP VI-NaTC-DOPC-SAN; (Eiii) SEM analysis of ASP VI; (Eiv) SEM analysis of ASP VI-NaTC-DOPC-SAN.

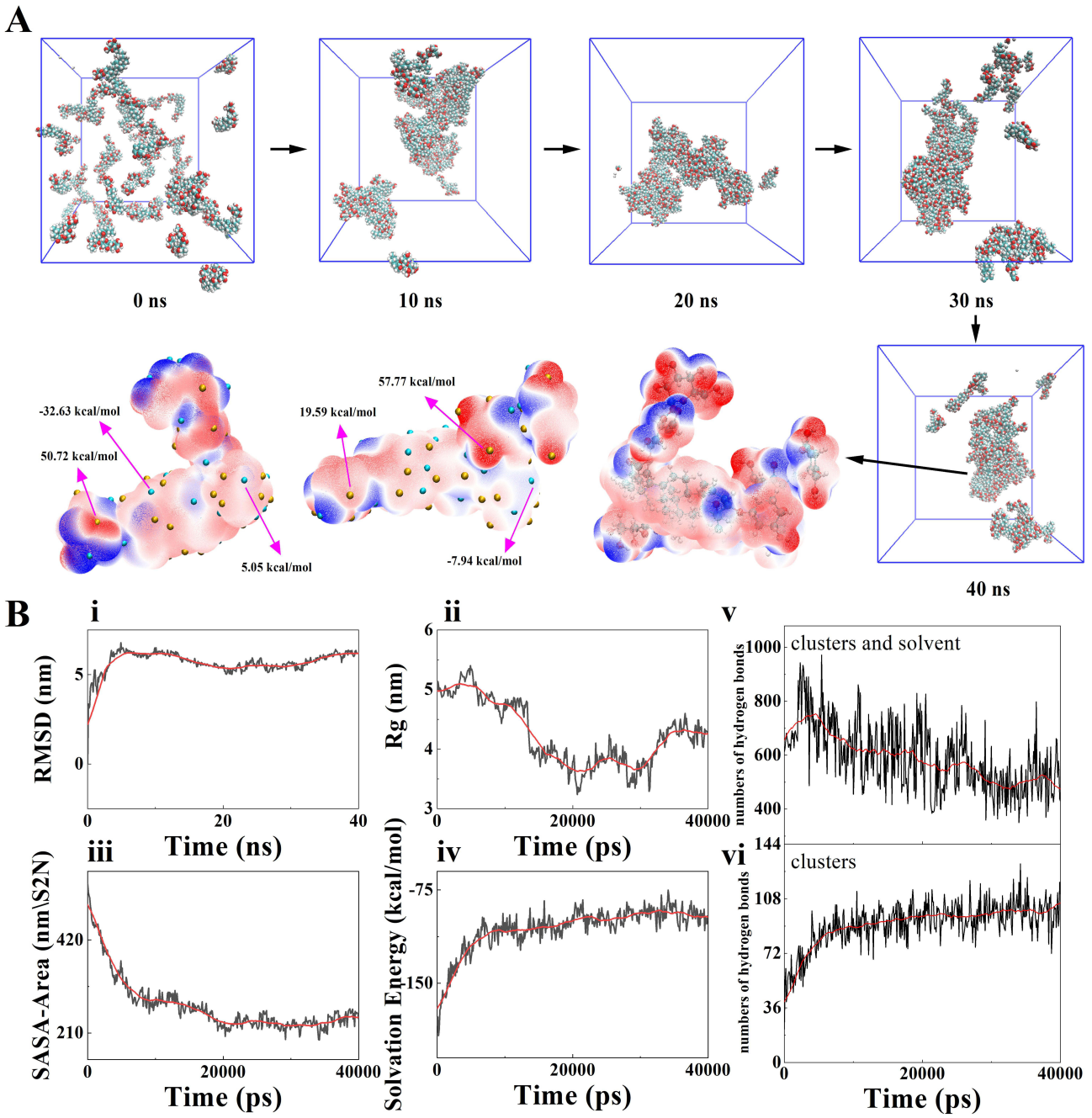

Figure 5 MDS of ASP VI self-assembly in aqueous solution. (**A**) ASP VI in aqueous solution system of molecular simulation trajectory, rod-shaped clusters appear in the 10 ns system, extraction of 40 ns system coordinates, clusters of two compounds in map molecular van der Waals surface electrostatic potential, red is potential, yellow ball corresponding potential maximum point, blue negative potential, the green ball corresponding electrostatic potential minimum point, Molecular binding sites indicate electrostatic potential values; (**B**) Data analysis of ASP VI in aqueous solution system simulation: (Bi) Compound clusters root mean square deviation (RMSD), (Bii) Cycloidal radius (Rg), (Biii) Solvent accessible surface Area (SASA-Area), (Biv) Solvation free energy (Solvation Energy), (Bv) Number of intermolecular hydrogen bonds of ASP VI in aqueous solution; (Bvi) Number of intermolecular hydrogen bonds of ASP VI and water molecules in aqueous solution.

solubility of ASP VI in aqueous solution was showed after self-assembly into rod-like clusters, compared with the amorphous ASP VI molecules (Figure 5Biv). It was noteworthy that only the monosaccharide ring of ASP VI was a binding site in aqueous solution for self-assembly while the disaccharide ring was not a binding site. After the formation of rod-shaped clusters, the hydrophilic group disaccharide rings are still exposed to the aqueous system, resulting in a nonsignificant increase in its permeability.

MDS of ASP VI Self-Assembly in Simulated Intestinal Fluid

MDS was performed to investigate the self-assembly of ASP VI into nanometer structures in simulated intestinal fluid. Based on the composition of the simulated intestinal fluid, 5 ASP VI molecules, 5 NaTC molecules and 3 DOPC molecules were randomly inserted into a 10×10×10 nm aqueous solution, and the system was equilibrated for energy, temperature, pressure and density (Figure S5). After the preparatory work was completed, the system was subjected to a 40 ns MDS, and it was found that rod-shaped clusters were formed by self-assembly of ASP VI, NaTC and DOPC molecules after 20 ns of simulation (Figure 6A). The results showed the electrostatic interaction was the driving force for the self-assembly of ASP VI and NaTC. However, DOPC had a weaker electrostatic potential and less electrostatic interaction with ASP VI. It is speculated that there may be other intermolecular interactions between them.

The data analysis results of the simulation process also indicated the formation of stable self-assembled nanometer structures in the system (Figure 6Bi–iii), with a decrease in solvation energy (Figure 6Biv) and an increase in the number of hydrogen bonds between cluster molecules (Figure 6Bv and vi). Specifically, NaTC interacts with ASP VI molecules through hydrogen bonding, while DOPC has no hydrogen bonding interactions with other compounds (Figure 6B and C). Therefore, it is believed that hydrophobic interaction is the main driving force for the self-assembly of DOPC and ASP VI. It is noteworthy that the monosaccharide and disaccharide rings at both ends of ASP VI act as key points to bind with

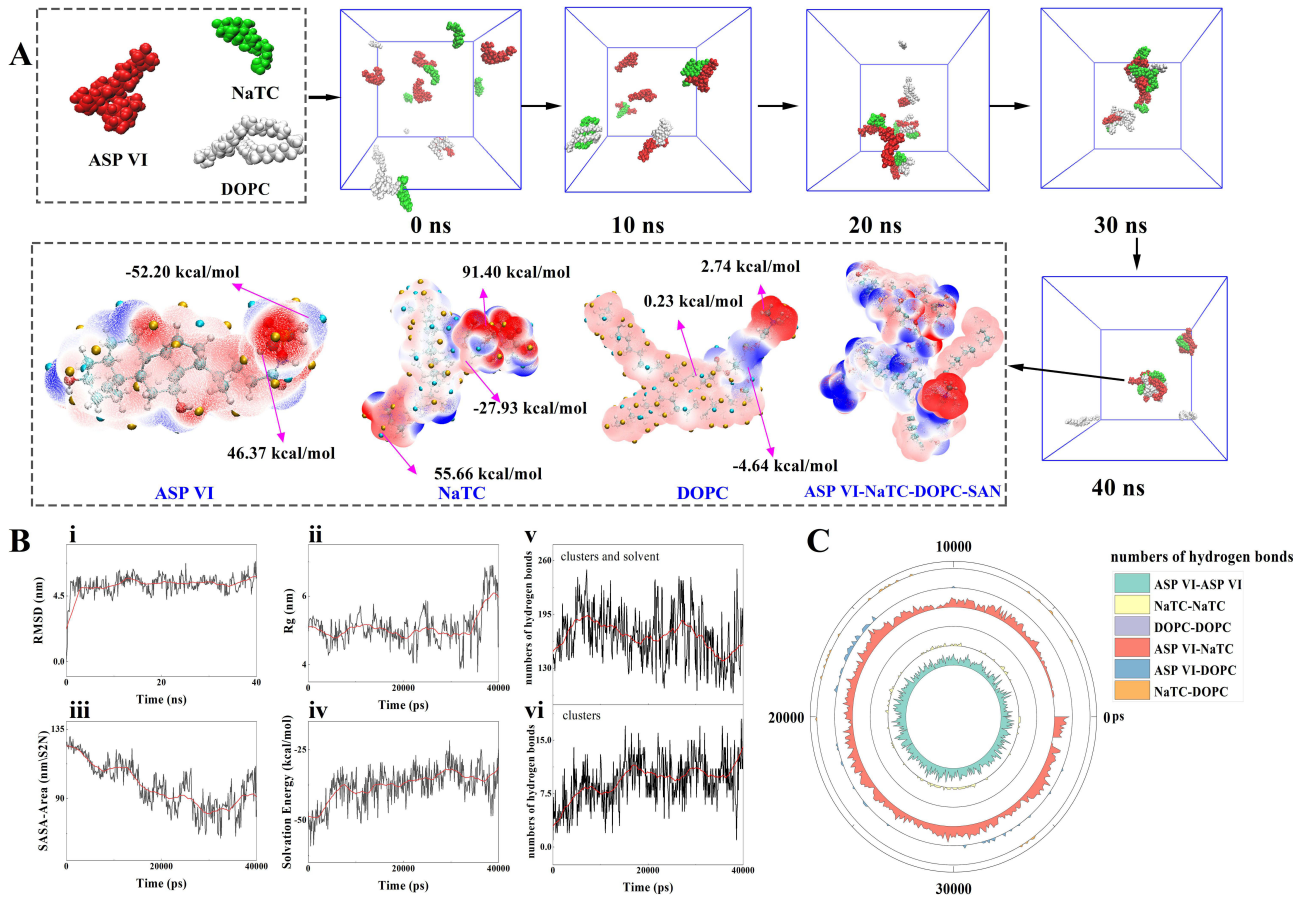

Figure 6 MDS of ASP VI self-assembly in simulated intestinal fluid. (**A**) ASP VI in simulated intestinal fluid system of molecular simulation, simulation system after 20 ns in rod clusters, extract the clusters in the 40 ns system of coordinates, three compounds map molecular van der Waals surface electrostatic potential, red is potential, yellow ball corresponding potential maximum point, blue negative potential, the green ball corresponding electrostatic potential minimum point, and molecular binding sites indicate electrostatic potential values; (**B**) Data analysis of ASP VI in simulated intestinal fluid system: (Bi) Root mean square deviation (RMSD), (Bii) Cycloidal radius (Rg), (Biii) Solvent accessible surface Area (SASA-Area), (Biv) Solvation free Energy (Solvation Energy), (Bv) Number of intermolecular hydrogen bonds of compounds in simulated intestinal fluid; (Bvi) Number of intermolecular hydrogen bonds between compounds and water molecules in simulated intestinal fluid. (**C**) Number of hydrogen bonds interacting with ASP VI, NaTC and DOPC in simulated intestinal fluid system (If the distance between donor and recipient is less than 4.0 and the corresponding Angle is greater than 120°, it is defined as a hydrogen bond).

NaTC and DOPC, resulting in hydrophilic groups located within rod-shaped clusters after self-assembly, greatly improving the permeability of the drug.

Phase Characterization of Self-Assembly

FT-IR Spectral Analysis

The FT-IR spectra analysis of NaTC, DOPC, ASP VI, Physical mixture (PM), and ASP VI -NaTC-DOPC-SAN were shown in Figure 7. All samples exhibit clear absorption peaks within the range of 3550 cm^{-1} to 2840 cm^{-1}. Specifically, the "O-H" stretching vibration is observed between 3550 cm^{-1} to 3200 cm^{-1}, while the "C-H" stretching vibration occurs within the range of 2950 cm^{-1} to 2840 cm^{-1}. The infrared spectral absorption of NaTC (Figure 7A) is characterized by the peaks at 3085 cm^{-1} and 1545 cm^{-1} correspond to the stretching vibration and bending vibration of "N-H", respectively. The peak at 1653 cm^{-1} represents the "C=O" stretching vibration. Additionally, the peak at 1466 cm^{-1} corresponds to the "O-H" bending vibration, while the peak at 1374 cm^{-1} corresponds to the "C-H" bending vibration. The peak at 1208 cm^{-1} represents the "C-N" stretching vibration. Furthermore, the peaks at 1045 cm^{-1} and 741 cm^{-1} correspond to the "S=O" stretching vibration and "C-S" stretching vibration of the sulfonic acid group, respectively.

DOPC exhibit several prominent peaks corresponding to different molecular vibrations (Figure 7B). These include the "C=O" stretching vibration at 1742 cm^{-1}, the "C=C" vibration at 1653 cm^{-1}, the "O-H" bending vibration at 1465 cm^{-1}, the "C-H" bending vibration at 1378 cm^{-1}, and the "C-O" stretching vibration at 1224 cm^{-1}. Additionally, peaks related to the stretching vibration of the "P=O" group can be observed at 1171 cm^{-1}, the "P=O" stretching vibration peak at 968 cm^{-1}, and the "P-O-C" stretching vibration near 824 cm^{-1}. The FT-IR spectral absorption of ASP VI (Figure 7C) exhibits characteristic peaks for "C=O" stretching vibration (1742 cm^{-1}), "C=C" (1653 cm^{-1}), "O-H" bending vibration (1465 cm^{-1}), "C-H" bending vibration (1378 cm^{-1}), "C-O" stretching vibration (1224 cm^{-1}), and "C-O-C" stretching vibration (1085 cm^{-1}).

The infrared spectrum of PM corresponds to the characteristic absorption peaks of NaTC, DOPC and ASP VI (Figure 7D). Furthermore, the absorption peaks in the infrared spectrum of ASP VI-NaTC-DOPC-SAN samples primarily correspond to the characteristic absorption peaks of ASP VI (Figure 7E). Based on the red shift phenomenon observed in the "O-H" stretching vibration, it can be inferred that the self-assembly process is primarily driven by hydrogen bonds, van der Waals forces, and other interactions between the host and guest. It is important to note that no new chemical bonds are formed during this process.[49] These findings are consistent with previous studies on the self-assembly mechanism of molecular dynamics simulations.

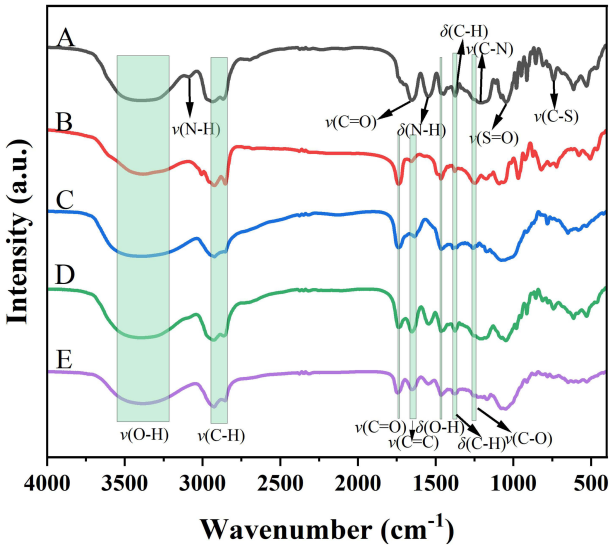

Figure 7 Fourier transform infrared spectral features. (A) NaTC; (B) DOPC; (C) ASP VI; (D) ASP VI-NaTC-DOPC-PM; (E) ASP VI-NaTC-DOPC-SAN.

TGA and DSC Analysis

The TG and DSC curves provided valuable information for understanding the changes in thermal stability and heat uptake of ASP VI, NaTC, DOPC, PM, and ASP VI-NaTC-DOPC-SAN micelles. The results of the DSC curve showed a sharp heat absorption peak at 373.9 °C for NaTC is observed in Figure 8A, corresponding to its melting and crystallization processes. DOPC and ASP VI are present in the amorphous phase with a broad heat absorption peak near 239.8 and 59.8°C, respectively (Figure 8B and C). The DSC curve of PM is basically the superposition of ASP VI with NaTC and DOPC (Figure 8D). Interestingly, the heat absorption peak of NaTC in PM was weakened, while the heat absorption capacity of DOPC and ASP VI was enhanced. It might be associated with temperature effects and material collisions.[50] Notably, no new heat absorption peaks appear in the ASP VI-NaTC-DOPC-SAN spectra (Figure 8E). Compared with the DSC curves of the PM, the DSC curve of the self-assembled micelles was smoother and the inflection points of the TGA curves did not change significantly, indicating that the molecular assemblies of ASP VI-NaTC-DOPC-SAN became more ordered and stable.[51] The TG analysis shows that the mass loss of ASP VI between 35 °C and 400 °C is 77.49% (Figure 8C). In comparison, the mass loss of ASP VI-NaTC-DOPC-SAN within the same temperature range is 58.15% (Figure 8E). This revealed that ASP VI-NaTC-DOPC-SAN exhibited greater thermal stability than ASP VI at the same temperature. This improved thermal stability can be attributed to the interaction between ASP VI and the endogenous components (NaTC and DOPC), which stabilize the overall structure of the micelles.

Self-Assembled Structures Promoting Absorption and Permeability of ASP VI

The storage stability and gastrointestinal stability of ASP VI-NaTC-DOPC-SAN were initially evaluated. Our results indicated that this micellar structure remained relatively stable when stored under hermetic conditions at 4 °C for 7 days

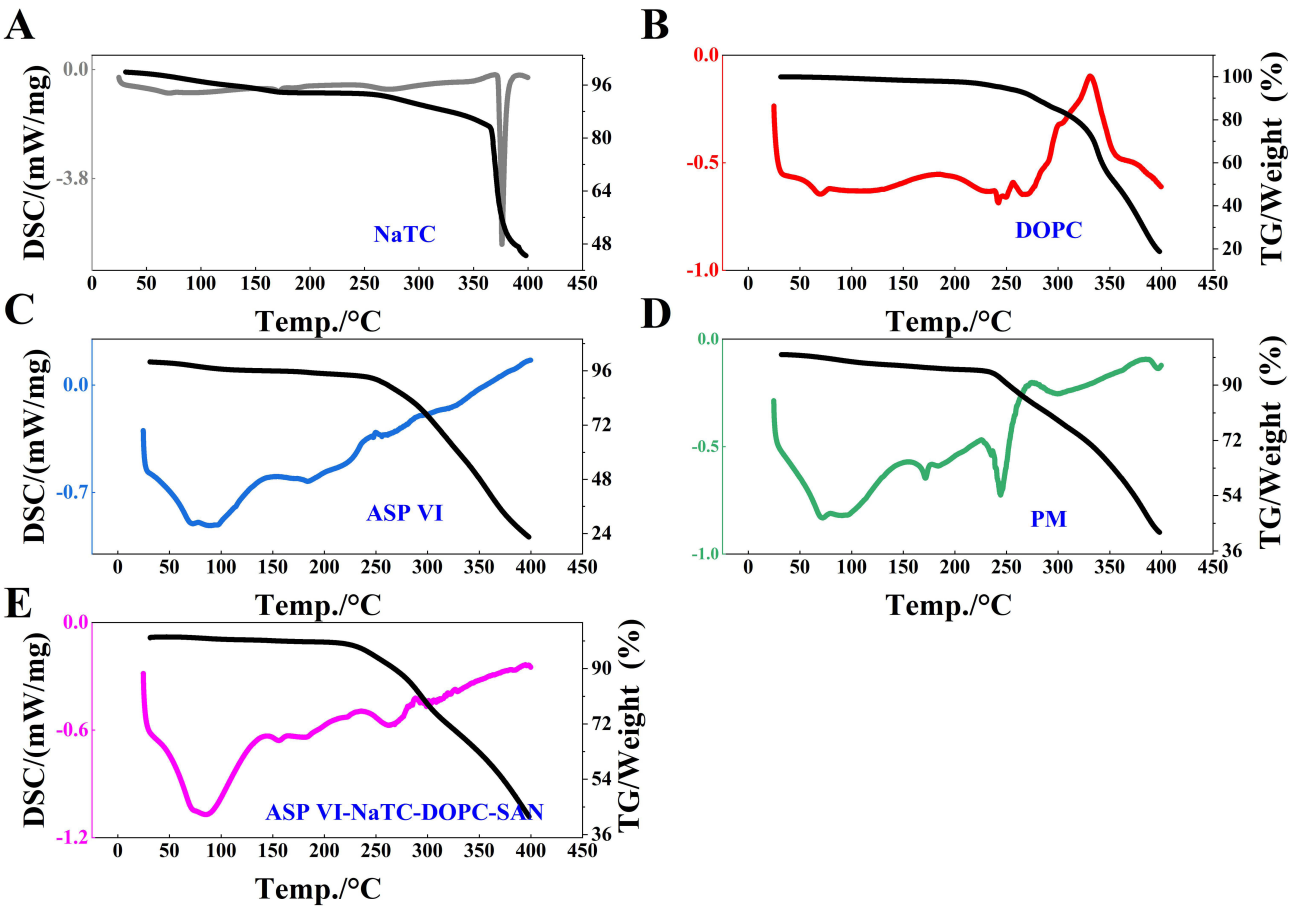

Figure 8 Characterization of the self-assembled nanomicelles. (**A**–**E**) correspond to DSC and TGA characteristics of NaTC, DOPC, ASP VI, PM and ASP VI-NaTC-DOPC-SAN, respectively. (The colored lines represent the DSC results for each group, while the black lines represent the TGA results).

(Figure S6). However, it was unstable when exposed to air or storage under hermetic conditions at 25°C, with aggregation and oxidative discoloration observed from the second day. Notably, the particle size and PDI remained relatively unchanged. Instead of undergoing digestion or degradation, ASP VI-NaTC-DOPC-SAN exhibited protonated aggregation in simulated gastric fluid, decreased-surface charge density of micelles, and increased-interaction forces, leading to aggregation of nanomicelles for increasing its PDI. In the presence of intestinal fluid, the micelles showed a normal surface charge density and maintained their initial particle size and PDI. All these results demonstrated that ASP VI-NaTC-DOPC-SAN is stable in the intestinal environment (Figure 9A). The PAMPA model was conducted to evaluate In vitro gastrointestinal (GIT) permeability.[52] Results shown in (Figure 9B and C), the effective permeability of ASP VI-NaTC-DOPC-SAN increased 13.33 times after 12 h compared to the self-assembled micelles formed by ASP VI in aqueous solution (1.71% ± 0.13 and 24.52% ± 1.86, respectively). Notably, the effective in vitro permeability of the free drug was slightly lower than the self-assembly of ASP VI in water. We speculated that this phenomenon might be due to the release of hydrophilic groups when the self-assembled structure of the ASP VI is disassembled in an acidic environment. However, this finding requires further validation.

Furthermore, a quadruple single-pass intestinal perfusion model was applied to evaluate the absorption of ASPVI-NaTC -DOPC-SAN in vivo. The results revealed that the absorption rate constant (K_a) (Figure 9D) and effective permeability coefficient (P_{eff}) (Figure 9E) of ASPVI-NaTC-DOPC-SAN were significantly increased in the duodenum, jejunum, ileum and colon, compared with the control group. Although studies have shown a low permeability of ASP VI, we found that ASP VI-NaTC-DOPC-SAN had a higher absorption rate and effective permeability coefficient in vivo, demonstrating that the self-assembled structure may improve significantly the drug's permeability. Additionally, the intestinal metabolic status of ASP VI was analyzed by injecting the intestinal perfusion samples into UPLC-Q-TOF-MS (Figure S7), and it was found to exist mainly in the form of prototype compounds without new metabolites, indicating its good stability in the gastrointestinal environment. Therefore, our findings indicated that endogenous components could be a crucial factor influencing the in vivo absorption and permeability of compounds with poor oral bioavailability.

Cellular Uptake, Internalization and Transport Mechanism

To further validate and confirm the interaction of self-assembled nanostructures with enterocytes, the dynamics of Caco-2 cell uptake were evaluated using DiO as a fluorescent tracer. Flow cytometry was used to quantify the uptake of Caco-2 cells by ASP VI and ASP VI-NaTC-DOPC-SAN (Figure S8). The results showed that the cellular uptake of ASP VI and ASP VI-NaTC-DOPC-SAN were in time-dependent (Figure 10A). The ASP VI and ASP VI-NaTC-DOPC-SAN solutions were labeled with Dio and incubated with Caco-2 cells for 1 hour. The relative cell absorption rates were 7.29% and 96.1%, respectively. In contrast, the cellular uptake rate of ASP VI-NaTC-DOPC-SAN was significantly increased by 13.18-fold, which is consistent with the results of PAMPA in vitro.

The main reasons for the permeability increasing of ASP VI due to the formation of nanomicelles is the monosaccharide and disaccharide rings at both ends of ASP VI are combined with NaTC and DOPC respectively, and the hydrophilic group is wrapped inside after self-assembly. The above micellar structure could produce a liposome-like uptake effect and showed strong intestinal epithelial permeability, thereby enhancing the permeability of ASP VI in vitro. The cellular uptake of ASP VI and ASP VI-NATC-DOPC-SAN in the presence of various inhibitors treated at 4 °C was shown in Figure 10B. Methyl β cyclodextrin and Chlorpromazine were used as nonspecific and specific clathrin-mediated endocytosis inhibitors, respectively. Methyl β cyclodextrin significantly markedly inhibited the uptake of ASP VI-NaTC-DOPC-SAN and ASP VI compared to the control, while chlorpromazine had minimal impact on the cellular uptake rate of both ASP VI-NaTC-DOPC-SAN and ASP VI. Simvastatin and genistein were treated as nonspecific and specific caveolin-mediated endocytosis inhibitors,[53] and they both significantly inhibited the cellular uptake of ASP VI. However, they had no significant inhibitory effect on the cellular uptake rate of ASP VI-NaTC-DOPC-SAN. Interestingly, at a low temperature of 4 °C, the cellular uptake of ASP VI and ASP VI-NaTC-DOPC-SAN was substantially reduced by 80.36% and 67.70%, respectively. These findings suggest that ASP VI and ASP VI-NaTC-DOPC-SAN employ different cellular uptake mechanisms. Clathrin-mediated endocytosis and nonspecific caveolin-mediated endocytosis were found to be involved in the uptake process of ASP VI. However, the specific inhibitors Amiloride (EIPA) and Dynasore, targeting macropinocytosis and actin respectively,[54] significantly inhibited the cellular uptake of ASP VI-NaTC-DOPC-SAN. Notably, EIPA had a lesser effect on ASP VI cellular uptake. These results

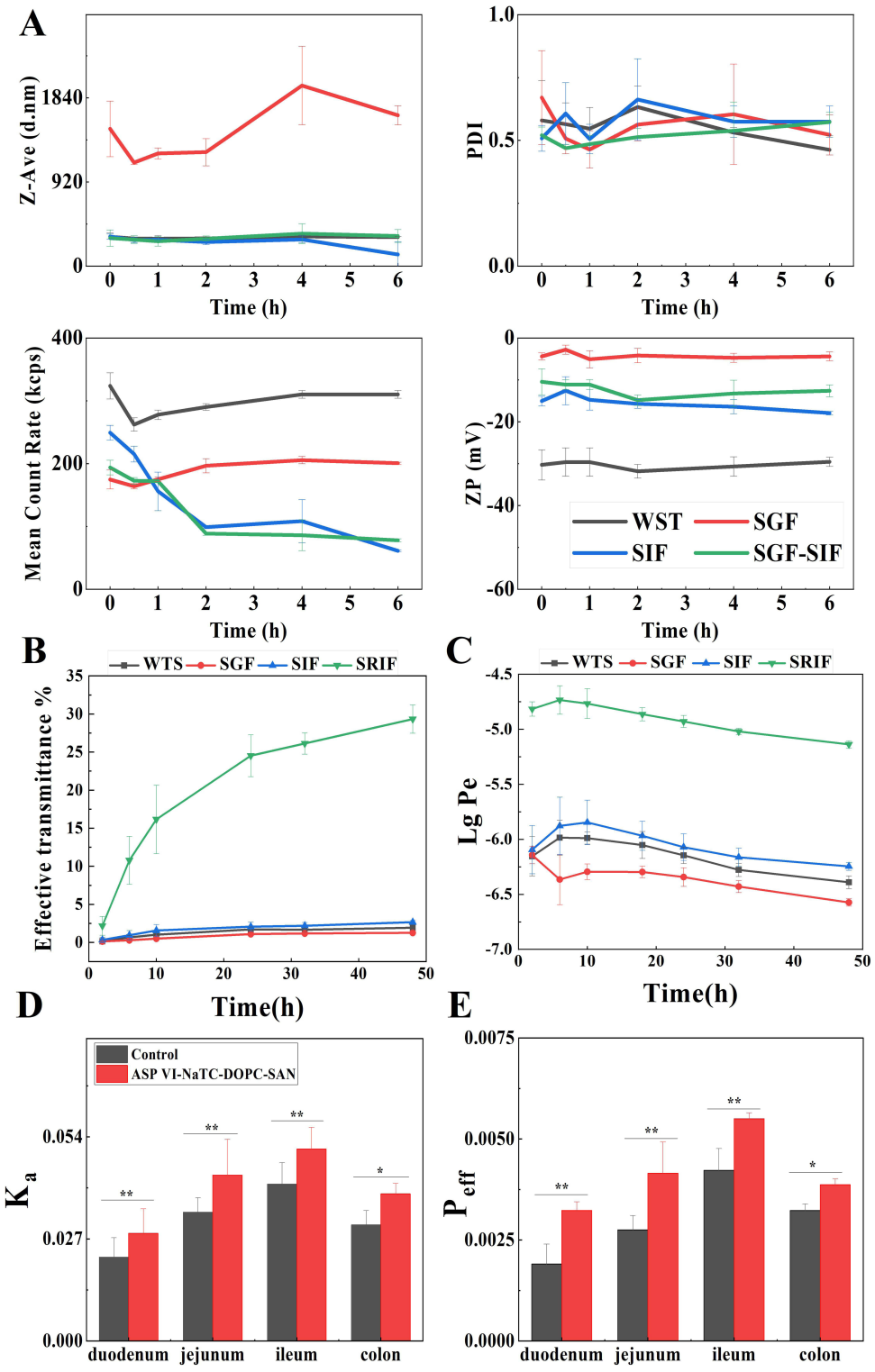

Figure 9 The promotion of self-assembly structure to the absorption and permeability of ASP VI. (**A**) DLS analysis of the gastrointestinal stability results of self-assembled nanomicelles in vitro; (**B** and **C**) Effective transmittance (T_{eff}) and effective permeability coefficient LgP_e of PAMPA; (**D** and **E**) Absorption rate constant (K_a) and effective permeability coefficient (P_{eff}) for intestinal perfusion in rats. Data are presented as means ± SD (n =3), ANOVA, Compared with control group, *$P < 0.05$, **$P < 0.01$.

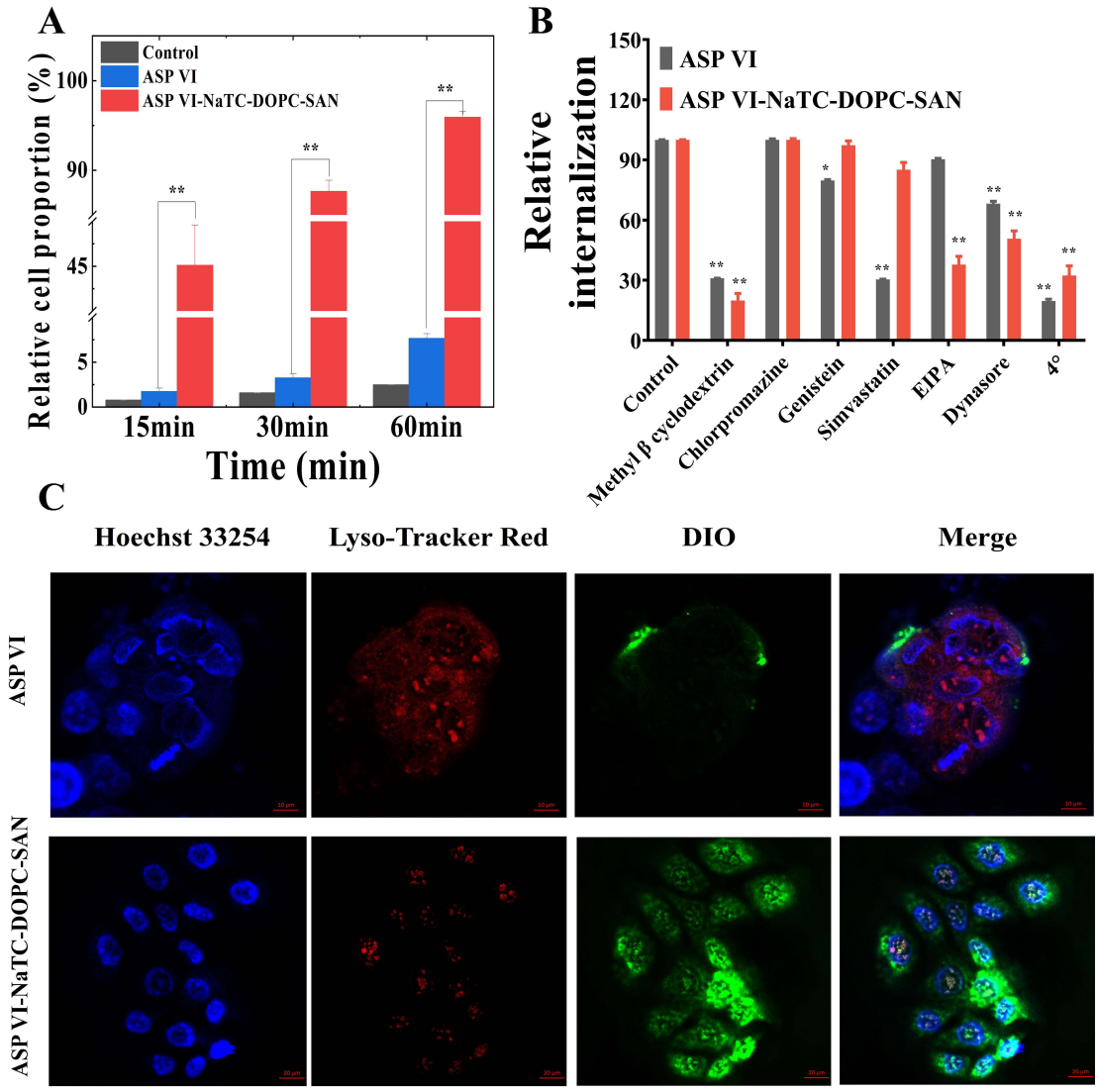

Figure 10 Time-dependence of cellular uptake study in Caco-2 cells for 15, 30 and 60 min. (**A**) Time-dependent uptake of DiO-labeled (10μM) ASP VI and ASP VI-NaTC-DOPC-SAN in Caco-2 cells; (**B**) Effects of endocytosis inhibitors on the cellular uptake of Caco-2 cells; (**C**) Confocal microscopy image of Caco-2 cells incubated with ASP VI and ASP VI-NaTC-DOPC-SAN for 1 h, Lysosomes were stained with Lysotracker Red (red), cell nuclei were stained with Hoechst 33254 (blue) and ASP VI and ASP VI-NaTC-DOPC-SAN were labeled by DiO (green). Compared with control group, $^{*}P < 0.05$, $^{**}P < 0.01$.

suggest that ATP-dependent transport via specific transporter proteins or cytosolic effects may play a primary role in the cellular uptake of ASP VI-NaTC-DOPC-SAN.

Some transporters are highly sensitive to temperature, leading to significant inhibition of active transport at lower temperatures. However, the specific transporter responsible for transporting ASP VI-NaTC-DOPC-SAN remains unidentified. Nevertheless, the active transport mechanism facilitates the assimilation of ASP VI-NaTC-DOPC-SAN by absorptive intestinal epithelial cells.

In CLSM imaging of endocytosis, it was obviously observed that ASP VI-NATC-DOPC-SAN associated green fluorescence was more diffuse in the cell colony at the same time, while ASP VI mainly gathered in the plasma membrane of cells (Figure 10C). The results of this study are consistent with our previous observation that self-assembled nanomicelles combined with endogenous NaTC and DOPC can promote intracellular delivery through the endocytosis pathway.[55] However, the low lysosomal colocalization of ASP VI may be related to its fossa mediated endocytosis pathway, which can evade fusion with lysosomes.[56]

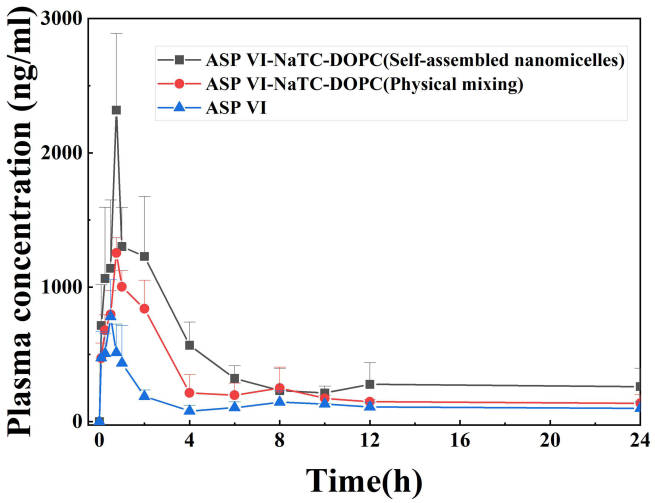

Figure 11 Plasma drug concentration-time curve of rats in ASP VI, ASP VI-NaTC-DOPC-PM, ASP VI-NaTC-DOPC-SAN groups after oral administration of 150 mg/kg ASP VI. (means ±SD, n = 5).

It has been reported previously that ASP VI can accumulate in aqueous solution[57] and thus alter the permeability of the cellular bypass, but there are no reports of its self-assembly in the human gastrointestinal environment. Additionally, it has been suggested that endogenous components such as NaTC and DOPC in the gastrointestinal environment can interact with the components of biopharmaceutics classification system class III with high solubility and low permeability to improve drug absorption and permeability.

Bioavailability Improvement of ASP VI

Pharmacokinetic studies (Tables S5–S7) were performed to compare the bioavailability of ASP VI, ASP VI-NaTC-DOPC-PM and ASP VI-NaTC-DOPC-SAN. The plasma concentration-time curves for the three groups showed a significant a double-peak phenomenon, which may be due to the role of bile acids in the enterohepatic circulation.[58] The T_{max} values for ASP VI-NaTC-DOPC-PM and ASP VI-NaTC-DOPC-SAN were identical at 0.63±0.13 h and 0.67 ±0.12 h, respectively. However, it was found that the plasma concentration–time curves of ASP VI- NaTC-DOPC-PM and ASP VI-NaTC-DOPC-SAN were found to be significant difference (Figure 11). At the same time, the absorption of ASP VI-NaTC-DOPC-SAN micelles was faster, and the increasing of C_{max} from 1.17 ± 0.17 μg/mL to 2.34 ± 0.26 μg/mL (Table 2). The relative bioavailability of ASP VI-NaTC-DOPC-SAN was 326.3%, which was significantly higher than the bioavailability of ASP VI.

There are possible reasons for the increase in absorption that can be attributed to two factors: Firstly, the hydrophilic groups of ASP VI were wrapped in self-assembled micelles, while endogenous components such as bile salts and phospholipids were able to act as membrane delivery enhancers and bind to membrane phospholipids, thereby increasing membrane permeability and promoting absorption.[59] Secondly, the formation process of ASP VI-NaTC-DOPC-SAN is

Table 2 Main Pharmacokinetic Parameters After Oral Administration of ASP VI, ASP VI-NaTC-DOPC-PM and ASP VI-NaTC-DOPC-SAN (150 Mg/Kg of ASP VI)

Parameter	Unit	ASP VI	ASP VI-NaTC-DOPC-PM	ASP VI -NaTC-DOPC-SAN
$t_{1/2}$	h	31.56±3.77	13.27±1.07	7.71±0.32
T_{max}	h	0.42±0.12	0.63±0.13	0.67±0.12
C_{max}	μg/mL	1.11±0.10	1.17±0.17	2.34±0.26**
AUC $_{0-t}$	μg/mL·h	3.89±0.73	5.74±1.48	12.54±2.54**
F	%	0.19±0.03	0.28±0.07	0.62±0.12**

Notes: Data expressed as means ± SD (n = 5). ANOVA, **$P < 0.01$, compared with ASP VI.

dynamic. The nanomicelles formed by ASP VI with endogenous components (NaTC and DOPC) were dispersed in the gastric acid environment and reassembled in the intestinal lumen to form nanomicelles with relatively homogeneous particle sizes, and ASP VI was homogeneously encapsulated in the combined micelles. Therefore, the drug molecules can be effectively controlled to maintain a certain concentration in the body, so that the absorption of the drug in the body is more durable.

Conclusion

Considering that the ambiguity of absorption and permeation mechanisms of active ingredients in TCM, our study adopted the spiral research mode of "phase structure-material basis-molecular mechanism-absorption and transportation" to explore the action mechanism of ASP VI in vivo. The present study aimed to unveil the formation mechanism of dynamic self-assembled nanomicelles of ASP VI, the primary active ingredient in Chinese medicine Dipsacus asperoides, in vivo. Furthermore, the study observed that NaTc-DOPC-VI-SAN significantly enhanced the Cmax and AUC0-t of ASP VI in vivo. Additionally, the in vitro Caco-2 cellular uptake assay demonstrated the interaction between NaTc-DOPC-VI-SAN and intestinal cells, which facilitated cellular absorption and uptake. The study also delved into the interaction mechanism between ASP VI and endogenous components (DOPC and NaTC) using multispectral techniques and molecular dynamics simulations. The findings revealed that ASP VI could spontaneously form nanomicelles with DOPC and NaTC through electrostatic and hydrophobic interactions. This suggests that the self-assembled nanostructures of orally administered drugs in vivo may play a crucial role in improving the oral bioavailability of TCM.

This study focuses on the interaction characteristics between small molecules and endogenous components in the body to investigate the mechanism of dynamic self-assembly of ASP VI, NaTC, and DOPC in the gastrointestinal environment. Interestingly, the study found that the formation of nanomicelles significantly enhance the biopharmaceutical properties of ASP VI. These findings provide a research foundation for the clinical application of ASP VI and offer guidance for the design of dosage forms. The study aligns with the principles of TCM and incorporates molecular mechanism analysis, which is in line with the concept of "precision treatment" in modern medicine. However, there are still limitations in this study. Further research is needed to understand the specific mechanism by which self-assembled nanomicelles promote the absorption and transport of ASP VI.

Abbreviations

ASP VI, asperosaponin VI; NaTC, sodium taurocholate; DOPC, dipalmitoyl phosphatidylcholine; ASP VI-NaTC-DOPC-SAN: ASP VI-NaTC-DOPC-self-assembled nanostructures; SAN, self-assembled nanostructures; DLS, dynamic light scattering; TEM, transmission electron microscope; MDS, molecular dynamics simulations; PE, pancreatic enzyme; EYPC, egg yolk phosphatidylcholine; DDC, dodecane; SGF, simulated gastric fluid; SDF, simulated duodenum fluid; SJF, simulated jejunum fluid; SIF, simulated ileum fluid; SCF, simulated colonic fluid; PDI, polydispersity index; SEM, scanning electron microscope; PM, physical mixture; TGA, thermogravimetric analysis; FT-IR: Fourier transform infrared spectroscopy; ESP, electrostatic potentials; K_a, absorption rate constant; P_{eff}, permeability coefficient; CLSM, confocal laser scanning microscopy; DiO: 3.3′-dioctadecyloxacarbocyanine perchlorate; FACS, flow cytometry; PAMPA, parallel artificial membrane permeation; SD, standard deviation; TCM, traditional Chinese medicine; DAS, *dipsacus asperoides* saponins; RMSD, root mean square deviation; SASA-Area, solvent-accessible surface area; ANOVA, analysis of variance; GIT, gastrointestinal.

Data Sharing Statement

All Data and materials for this research is available directly to the corresponding author (Xiaobin Jia) on rational requests.

Consent for Publication

All authors have reviewed and consented to the submission of this manuscript. This manuscript has not been published in other publications.

Acknowledgments

This research was sponsored by the National Natural Science Foundation of China [project number: 82230117,recipient: Xiaobin Jia],Jiangsu Province Science and Technology Achievement Transformation Special Funds Program [project number: BA2020077,recipient: Jun Liu],Jiangsu Graduate Student Research Innovation Program [project number: KYCX23_0871,recipient: Yanjun Yang] and Jiangsu Funding Program for Excellent Postdoctoral Talent [project number: 2022ZB317 and 2023ZB824,recipient: Bing Yang and Zhiwei Xiong].

Author Contributions

All authors have made significant contributions to the reported work, including the conception, study design, execution, data acquisition, analysis and interpretation. They have also participated in drafting, revising, and critically reviewing the article. The authors have given their final approval for the version to be published and have agreed on the journal to which the article has been submitted. Furthermore, they accept accountability for all aspects of the work. We would like to thank all the authors for their contributions to this manuscript.

Disclosure

The authors declare that the study was implemented in the absence of any business or financial relationships that could be regarded as a potential conflict of interest.

References

1. Liu J, Li S, Liu L, et al. A fluorous biphase drug delivery system triggered by low frequency ultrasound: controlled release from perfluorous discoidal porous silicon particles. *Nanoscale Adv*. 2020;2(8):3561–3569. doi:10.1039/d0na00324g
2. Ejaz S, Hogg B, Hristov DR, et al. Add sugar to chitosan: mucoadhesion and in vitro intestinal permeability of mannosylated chitosan nanocarriers. *Pharmaceutics*. 2022;14(4):830. doi:10.3390/pharmaceutics14040830
3. Yeo S, Song HH, Kim MJ, et al. Synthesis and design of purpurin-18-loaded solid lipid nanoparticles for improved anticancer efficiency of photodynamic therapy. *Pharmaceutics*. 2022;14(5):1064. doi:10.3390/pharmaceutics14051064
4. Kulkarni VR, Kazi M, Shahba AA, et al. Three-dimensional printing of a container tablet: a new paradigm for multi-drug-containing bioactive self-nanoemulsifying drug-delivery systems (Bio-SNEDDSs). *Pharmaceutics*. 2022;14(5):1082. doi:10.3390/pharmaceutics14051082
5. Haggag YA, Ibrahim RR, Hafiz AA. Design, formulation and in vivo evaluation of novel honokiol-loaded PEGylated PLGA nanocapsules for treatment of breast cancer. *Int J Nanomed*. 2020;15:1625–1642. doi:10.2147/IJN.S241428
6. Park JY, Hyun JS, Jee JG, et al. Structural deformation of MTX induced by nanodrug conjugation dictate intracellular drug transport and drug efficacy. *Int J Nanomed*. 2021;16:4943–4957. doi:10.2147/IJN.S317231
7. Kim ES, Baek Y, Yoo HJ, et al. Chitosan-tripolyphosphate nanoparticles prepared by ionic gelation improve the antioxidant activities of astaxanthin in the in vitro and in vivo model. *Antioxidants*. 2022;11(3):479. doi:10.3390/antiox11030479
8. Qiao L, Yang H, Gao S, et al. Research progress on self-assembled nanodrug delivery systems. *J Mater Chem B*. 2022;10(12):1908–1922. doi:10.1039/d1tb02470a
9. Yu X, Xu H, Hu M, et al. Ginsenoside Rg3 bile salt-phosphatidylcholine-based mixed micelles: design, characterization, and evaluation. *Chem Pharm Bull*. 2015;63(5):361–368. doi:10.1248/cpb.c15-00045
10. Yu JN, Zhu Y, Wang L, et al. Enhancement of oral bioavailability of the poorly water-soluble drug silybin by sodium cholate/phospholipid-mixed micelles. *Acta Pharmacol Sin*. 2010;31(6):759–764. doi:10.1038/aps.2010.55
11. Zhang H, Zhao L, Chu L, et al. Preparation, optimization, characterization and cytotoxicity in vitro of Baicalin-loaded mixed micelles. *J Colloid Interface Sci*. 2014;434:40–47. doi:10.1016/j.jcis.2014.07.045
12. Xu J, Karra V, Large DE, et al. Understanding the mechanical properties of ultradeformable liposomes using molecular dynamics simulations. *J Phys Chem B*. 2023;127(44):9496–9512. doi:10.1021/acs.jpcb.3c04386
13. Ke K, Li Q, Yang X, et al. Asperosaponin VI promotes bone marrow stromal cell osteogenic differentiation through the PI3K/AKT signaling pathway in an osteoporosis model. *Sci Rep*. 2016;6(1):35233. doi:10.1038/srep35233
14. Chen F, Liang Q, Mao L, et al. Synergy effects of Asperosaponin VI and bioactive factor BMP-2 on osteogenesis and anti-osteoclastogenesis. *Bioact Mater*. 2021;10:335–344. doi:10.1016/j.bioactmat.2021.09.001
15. Liu Q, Zhang J, Xiao C, et al. Akebia saponin D protects hippocampal neurogenesis from microglia-mediated inflammation and ameliorates depressive-like behaviors and cognitive impairment in mice through the PI3K-Akt pathway. *Front Pharmacol*. 2022;13:927419. doi:10.3389/fphar.2022.927419
16. Kamyab E, Goebeler N, Kellermann MY, et al. Anti-fouling effects of saponin-containing crude extracts from tropical indo-pacific sea cucumbers. *Mar Drugs*. 2020;18(4):181. doi:10.3390/md18040181
17. Zhi K, Zhao H, Yang X, et al. Natural product gelators and a general method for obtaining them from organisms. *Nanoscale*. 2018;10(8):3639–3643. doi:10.1039/c7nr08368h
18. Cheng JJ, Yang X. Self-assembly performance of triterpene natural small molecules and their application in synergistic antitumor chemotherapy. *Acta Pharm Sin*. 2021;56(08):2102–2111. doi:10.16438/j.0513-4870.2021-0617
19. Lin X, Huang X, Tian X, et al. Natural small-molecule-based carrier-free self-assembly library originated from traditional Chinese herbal medicine. *ACS Omega*. 2022;7(48):43510–43521. doi:10.1021/acsomega.2c04098

20. Brodkorb A, Egger L, Alminger M, et al. INFOGEST static in vitro simulation of gastrointestinal food digestion. *Nat Protoc*. 2019;14(4):991–1014. doi:10.1038/s41596-018-0119-1
21. Minekus M, Alminger M, Alvito P, et al. A standardised static in vitro digestion method suitable for food-an international consensus. *Food Funct*. 2014;5(6):1113–1124. doi:10.1039/c3fo60702j
22. Skalickova S, Ridoskova A, Slama P, et al. Effect of lactic fermentation and cooking on nutrient and mineral digestibility of peas. *Front Nutr*. 2022;9:838963. doi:10.3389/fnut.2022.838963
23. Clulow AJ, Parrow A, Hawley A, et al. Characterization of solubilizing nanoaggregates present in different versions of simulated intestinal fluid. *J Phys Chem B*. 2017;121(48):10869–10881. doi:10.1021/acs.jpcb.7b08622
24. Xiong Q, Jiang Y, Cai X, et al. Conformation dependence of diphenylalanine self-assembly structures and dynamics: insights from hybrid-resolution simulations. *ACS Nano*. 2019;13(4):4455–4468. doi:10.1021/acsnano.8b09741
25. Malde AK, Zuo L, Breeze M, et al. An automated force field topology builder (ATB) and repository: version 1.0. *J Chem Theory Comput*. 2011;7(12):4026–4037. doi:10.1021/ct200196m
26. Stroet M, Caron B, Visscher KM, Geerke DP, Malde AK, Mark AE. automated topology builder version 3.0: prediction of solvation free enthalpies in water and hexane. *J Chem Theory Comput*. 2018;14(11):5834–5845. doi:10.1021/acs.jctc.8b00768
27. Fábián B, Thallmair S, Hummer G. Optimal bond constraint topology for molecular dynamics simulations of cholesterol. *J Chem Theory Comput*. 2023;19(5):1592–1601. doi:10.1021/acs.jctc.2c01032
28. Karwasra R, Fatihi S, Raza K, et al. Filgrastim loading in PLGA and SLN nanoparticulate system: a bioinformatics approach. *Drug Dev Ind Pharm*. 2020;46(8):1354–1361. doi:10.1080/03639045.2020.1788071
29. Miller RE, Tadmor EB, Gibson JS, et al. Molecular dynamics at constant Cauchy stress. *J Chem Phys*. 2016;144(18):184107. doi:10.1063/1.4948711
30. Martonák R, Laio A, Parrinello M. Predicting crystal structures: the Parrinello-Rahman method revisited. *Phys Rev Lett*. 2003;90(7):075503. doi:10.1103/PhysRevLett.90.075503
31. Bisong EA, Louis H, Unimuke TO, et al. Vibrational, electronic, spectroscopic properties, and NBO analysis of p-xylene, 3,6-difluoro-p-xylene, 3,6-dichloro-p-xylene and 3,6-dibromo-pxylene: DFT study. *Heliyon*. 2020;6(12):e05783. doi:10.1016/j.heliyon.2020.e05783
32. Piazzini V, Rosseti C, Bigagli E, et al. Prediction of permeation and cellular transport of Silybum marianum extract formulated in a nanoemulsion by using PAMPA and Caco-2 cell models. *Planta Med*. 2017;83(14–15):1184–1193. doi:10.1055/s-0043-110052
33. Navarro Del Hierro J, Piazzini V, Reglero G, Martin D, Bergonzi MC. In vitro permeability of saponins and sapogenins from seed extracts by the parallel artificial membrane permeability assay: effect of in vitro gastrointestinal digestion. *J Agric Food Chem*. 2020;68(5):1297–1305. doi:10.1021/acs.jafc.9b07182
34. Dahlgren D, Roos C, Peters K, et al. Evaluation of drug permeability calculation based on luminal disappearance and plasma appearance in the rat single-pass intestinal perfusion model. *Eur J Pharm Biopharm*. 2019;142:31–37. doi:10.1016/j.ejpb.2019.06.011
35. Yao ZH, Qin ZF, He LL, et al. Identification, bioactivity evaluation and pharmacokinetics of multiple components in rat serum after oral administration of Xian-Ling-Gu-Bao capsule by ultra performance liquid chromatography coupled with quadrupole time-of-flight tandem mass spectrometry. *J Chromatogr B Analyt Technol Biomed Life Sci*. 2017;1041–1042:104–112. doi:10.1016/j.jchromb.2016.12.026
36. Wu A, Chen Y, Wang H, et al. Genetically-engineered "all-in-one" vaccine platform for cancer immunotherapy. *Acta Pharm Sin B*. 2021;11(11):3622–3635. doi:10.1016/j.apsb.2021.06.001
37. Li Y, Ji W, Peng H, et al. Charge-switchable zwitterionic polycarboxybetaine particle as an intestinal permeation enhancer for efficient oral insulin delivery. *Theranostics*. 2021;11(9):4452–4466. doi:10.7150/thno.54176
38. Herrera T, Navarro Del Hierro J, Fornari T, Reglero G, Martin D. Acid hydrolysis of saponin-rich extracts of quinoa, lentil, fenugreek and soybean to yield sapogenin-rich extracts and other bioactive compounds. *J Sci Food Agric*. 2019;99(6):3157–3167. doi:10.1002/jsfa.9531
39. Duan D, Doak AK, Nedyalkova L, et al. colloidal aggregation and the in vitro activity of traditional Chinese medicines. *ACS Chem Biol*. 2015;10(4):978–988. doi:10.1021/cb5009487
40. Parekh PY, Patel VI, Khimani MR, Bahadur P. Self-assembly of bile salts and their mixed aggregates as building blocks for smart aggregates. *Adv Colloid Interface Sci*. 2023;312:102846. doi:10.1016/j.cis.2023.102846
41. Tang XY, Dai ZQ, Wu QC, et al. Simultaneous determination of multiple components in rat plasma and pharmacokinetic studies at a pharmacodynamic dose of Xian-Ling-Gu-Bao capsule by UPLC-MS/MS. *J Pharm Biomed Anal*. 2020;177:112836. doi:10.1016/j.jpba.2019.112836
42. Sun X, Zhang Y, Yang Y, et al. Qualitative and quantitative analysis of furofuran lignans, iridoid glycosides, and phenolic acids in Radix Dipsaci by UHPLC-Q-TOF/MS and UHPLC-PDA. *J Pharm Biomed Anal*. 2018;154:40–47. doi:10.1016/j.jpba.2018.03.002
43. Pal S, Medatwal N, Kumar S, et al. A localized chimeric hydrogel therapy combats tumor progression through alteration of sphingolipid metabolism. *ACS Cent Sci*. 2019;5(10):1648–1662. doi:10.1021/acscentsci.9b00551
44. Zheng J, Fan R, Wu H, et al. Directed self-assembly of herbal small molecules into sustained release hydrogels for treating neural inflammation. *Nat Commun*. 2019;10(1):1604. doi:10.1038/s41467-019-09601-3
45. Ma Z, Cai D, Yang S, Li Y, Li Y. Enhancement of interfacial charge transfer of TiO 2 /graphene with Doped Ca 2+ for improving electrical conductivity. *ACS Appl Mater Interfaces*. 2021;13(35):41875–41885. doi:10.1021/acsami.1c07401
46. Park J, Kravchuk P, Krishnaprasad A, Roy T, Kang EH. Graphene enhances actin filament assembly kinetics and modulates NIH-3T3 fibroblast cell spreading. *Int J Mol Sci*. 2022;23(1):509. doi:10.3390/ijms23010509
47. Abraham MJ, Murtola T, Schulz R, et al. GROMACS: high performance molecular simulations through multi-level parallelism from laptops to supercomputers. *SoftwareX*. 2015;1–2:19–25. doi:10.1016/J.SOFTX.2015.06.001
48. Koder Hamid M, Månsson LK, Meklesh V, Persson P, Skepö M. Molecular dynamics simulations of the adsorption of an intrinsically disordered protein: force field and water model evaluation in comparison with experiments. *Front Mol Biosci*. 2022;9:958175. doi:10.3389/fmolb.2022.958175
49. Benesch MG, Mannock DA, Lewis RN, McElhaney RN. A DSC and FTIR spectroscopic study of the effects of the epimeric 4-cholesten-3-ols and 4-cholesten-3-one on the thermotropic phase behaviour and organization of dipalmitoylphosphatidylcholine bilayer membranes: comparison with their 5-cholesten analogues. *Chem Phys Lipids*. 2014;177:71–90. doi:10.1016/j.chemphyslip.2013.11.008
50. Mudgil D, Barak S, Khatkar BS. X-ray diffraction, IR spectroscopy and thermal characterization of partially hydrolyzed guar gum. *Int J Biol Macromol*. 2012;50(4):1035–1039. doi:10.1016/j.ijbiomac.2012.02.031

51. Wang RH, Ding BT, Liang GZ. Interaction poses, intermolecular forces, dynamic preferences between flavonoids and maltosyl-β-cyclodextrin. *J Mol Liq*. 2022;346:117068. doi:10.1016/j.molliq.2021.117068
52. Wiergowska G, Stasiłowicz A, Miklaszewski A, Lewandowska K, Cielecka-Piontek J. Structural polymorphism of sorafenib tosylate as a key factor in its solubility differentiation. *Pharmaceutics*. 2021;13(3):384. doi:10.3390/pharmaceutics13030384
53. Rennick JJ, Johnston APR, Parton RG. Key principles and methods for studying the endocytosis of biological and nanoparticle therapeutics. *Nat Nanotechnol*. 2021;16(3):266–276. doi:10.1038/s41565-021-00858-8
54. Zhang P, Cheetham AG, Lin YA, Cui H. Self-assembled Tat nanofibers as effective drug carrier and transporter. *ACS Nano*. 2013;7(7):5965–5977. doi:10.1021/nn401667z
55. Ran W, Liu X, Chang L, et al. Self-assembling mertansine prodrug improves tolerability and efficacy of chemotherapy against metastatic triple-negative breast cancer. *J Control Release*. 2020;318:234–245. doi:10.1016/j.jconrel.2019.12.027
56. Parton RG, Simons K. The multiple faces of caveolae. *Nat Rev Mol Cell Biol*. 2007;8(3):185–194. doi:10.1038/nrm2122
57. Wang Y, Shen J, Yang X, et al. Mechanism of enhanced oral absorption of akebia saponin D by a self-nanoemulsifying drug delivery system loaded with phospholipid complex. *Drug Dev Ind Pharm*. 2019;45(1):124–129. doi:10.1080/03639045.2018.1526183
58. Xiang J, Zhang Z, Xie H, et al. Effect of different bile acids on the intestine through enterohepatic circulation based on FXR. *Gut Microbes*. 2021;13(1):1949095. doi:10.1080/19490976.2021.1949095
59. Zhong W, Jiang L, Wang X, Huang A, Li L, Ma L. Membrane structural change of dimyristoylphosphatidylcholine liposome on the interaction with polyethyleneimine. *Colloids Surf B Biointerfaces*. 2018;167:509–515. doi:10.1016/j.colsurfb.2018.04.054